Optical tomographic imaging of dynamic features of dense-scattering media

Randall L. Barbour

Department of Pathology, SUNY Downstate Medical Center, Box 25, 450 Clarkson Avenue, Brooklyn, New York 11203, and Department of Electrical Engineering, Polytechnic University, 6 Metrotech Center, Brooklyn, New York 11201

Harry L. Graber

Department of Pathology, SUNY Downstate Medical Center, Box 25, 450 Clarkson Avenue, Brooklyn, New York 11203

Yaling Pei

Department of Civil Engineering, Polytechnic University, 6 Metrotech Center, Brooklyn, New York 11201

Sheng Zhong

Department of Electrical Engineering, Polytechnic University, 6 Metrotech Center, Brooklyn, New York 11201

Christoph H. Schmitz

Department of Pathology, SUNY Downstate Medical Center, Box 25, 450 Clarkson Avenue, Brooklyn, New York 11203

Received October 19, 2000; accepted January 10, 2001; revised manuscript received March 16, 2001

Methods used in optical tomography have thus far proven to produce images of complex target media (e.g., tissue) having, at best, relatively modest spatial resolution. This presents a challenge in differentiating artifact from true features. Further complicating such efforts is the expectation that the optical properties of tissue for any individual are largely unknown and are likely to be quite variable due to the occurrence of natural vascular rhythms whose amplitudes are sensitive to a host of autonomic stimuli that are easily induced. We recognize, however, that rather than frustrating efforts to validate the accuracy of image features, the time-varying properties of the vasculature can be exploited to aid in such efforts, owing to the known structure-dependent frequency response of the vasculature and to the fact that hemoglobin is a principal contrast feature of the vasculature at near-infrared wavelengths. To accomplish this, it is necessary to generate a time series of image data. In this report we have tested the hypothesis that through analysis of time-series data, independent contrast features can be derived that serve to validate, at least qualitatively, the accuracy of imaging data, in effect establishing a self-referencing scheme. A significant finding is the observation that analysis of such data can produce *high-contrast* images that reveal features that are mainly obscured in individual image frames or in time-averaged image data. Given the central role of hemoglobin in tissue function, this finding suggests that a wealth of new features associated with vascular dynamics can be identified from the analysis of time-series image data.

OCIS codes: 100.2960, 170.3880, 100.2980, 170.4580, 100.6950, 170.5380.

1. INTRODUCTION

Interest in optical tomography continues to grow, largely because of its perceived potential for creating new venues for investigating functional features of critical organ systems in a wide range of clinical situations.[1] One area of interest is the use of optical tomography for the purpose of defining spatial variations in perfusion states (i.e., the level and oxygenation state of tissue hemoglobin).[2,3] Favoring such investigations is the fact that in the near infrared (NIR) region, hemoglobin is a principal contrast agent. While such sensitivity is desirable, the known dynamic behavior of the vasculature[4] can, depending on the conditions of measurement, be expected to give rise to considerable signal variability.[5] Interestingly, although such behavior is widely known,[6–8] its influence on image quality, and on information derivable from image data, has not been widely considered for the problem of optical tomography.

A brief consideration suggests that there are three options available for data collection that can be expected to influence the impact that vascular reactivity may have on image data. One would be to simply eliminate its influence by collecting data on a time frame that is long compared with the (reciprocal of the) lowest significant vascular frequency. Conversely, data could be collected on a fast time frame, thereby achieving a "snapshot." The third would be to collect a time series of images. Determining which of these alternatives is most suitable requires con-

sideration of related issues. For instance, confounding any choice is the relatively low spatial resolution of the images of tissue that have thus far been reported.[9–11] How much of this is due to underlying vascular reactivity, how much to limitations on data collection, and how much to numerical difficulties associated with image recovery (e.g., ill-posedness) is unclear. These considerations lead to an even more basic yet related question. Given that the optical properties of tissue are mainly unknown, and are time-varying (at least for absorption due to hemoglobin), how does one distinguish between possible artifacts present in the image data and real tissue contrast features that are recovered with low resolution?

A standard approach would be to simply compare optical contrast maps with some other data set, for example, a magnetic resonance (MR) image of the same site. While this can prove useful, the contrast mechanisms of MR (magnetic properties of hydrogen), and of other imaging methods for that matter, are very different from those at NIR wavelengths (absorption, mainly due to hemoglobin, and elastic light scatter, caused by differences in refractive index among subcellular structures). Hence, it could prove difficult from examination of low-resolution optical images to recognize features that are evident in other imaging modalities or to distinguish what is real from artifact. Adding to this the additional variability that, depending on measurement conditions, can arise from vascular reactivity serves to underscore the need for careful selection of data collection strategies.

It is our view that rather than frustrating efforts to validate the accuracy of image features, the time-varying properties of the vasculature can be exploited to aid in such efforts and to effect what amounts to a self-referencing scheme. The idea here is as follows. We recognize that various vascular structures, (e.g., arteries, veins, microvessels) exhibit particular natural beat frequencies, and in many instances the location of these structures in tissue is either well known or easily determined (e.g., from MR image data). Thus two different classes of information should be available from optical measurements: spatial maps revealing hemodynamic states (i.e., position-dependent tissue blood volume and blood oxygenation), and maps that reveal the temporal properties of these parameters (assuming an appropriate time series of image data is collected). Hence, by correlating the measured temporal features to the parameter maps, the accuracy of specific features can be verified, at least qualitatively. For instance, a cardiac frequency should be limited mainly to the major arteries. Should significant inconsistencies be found, it might suggest problems associated with data collection, image reconstruction, or some other factor.

We therefore consider the known structure-dependent frequency response of the vasculature tree to represent a fortuitous feature that can allow for the assignment of dynamic features to specific anatomic landmarks. We also recognize that this scheme need not be limited to dynamic features that occur at rest, or even to those that occur naturally. For instance, the coincidence of dynamic features with specific anatomic structures in response to various provocations can also be considered. Thus it is our view that the underlying vascular reactivity of tissue can be taken as an independent contrast feature that can aid in validating the accuracy of image results, and as a parameter domain whose particulars could prove especially relevant to understanding a range of physiological states.

In a series of recent preliminary reports, we have taken a first step toward exploring this interesting relationship in laboratory phantoms[12] and on the human forearm.[13–16] Here our goal has been to systematically explore, under controlled conditions, the nature and quality of information derivable from media made to experience dynamic behavior in their optical properties. In one case the test medium examined was an MR map of the breast, containing an included tumor, to which we assigned temporal variations in the optical properties of the different tissue types. In another case we examined a laboratory phantom containing four inclusions, two of which we made dynamic. Results obtained demonstrate that measures of temporal properties can serve to significantly enhance the detectability of included objects that may otherwise be obscured by the low spatial resolution of reconstructed images.

2. METHODS

A. Simulation Studies

1. Modeling of Tissue Hemodynamics in an MR Breast Map

Figure 1 shows a finite element model of the MR breast map used in these studies. Three different tissue types are identified: adipose (dark gray), parenchyma (light gray), and a centrally positioned tumor (black region). For convenience we have extended the external boundary of the actual breast map to conform to a circular geometry having a diameter of 8 cm. Hemodynamic parameters assigned to the segmented tissue types are listed in Table

Fig. 1. Medium used in simulation experiments. This finite element mesh was derived from a coronal section of a MR mammogram, following segmentation into three tissue types.

Table 1. Mean Values of the Tissue Blood Volume and Hemoglobin Oxygen Saturation, and Modulation Frequencies Assigned to Each Tissue Type in the Dynamic Simulations

Tissue Type	Fractional Blood Volume (V_b)	Hemoglobin Fractional Oxygen Saturation (S_{O_2})	Modulation Frequency (Hz)
Adipose Tissue	0.025	1.0	0.12
Parenchymal Tissue	0.035	0.9	0.40
Tumor	0.1	0.5	0.06

1. For each tissue type, a different mean value for tissue blood volume (V_b) (i.e., the fraction of the tissue volume that consists of blood) and oxygen saturation level (S_{O_2}) was assigned. The levels assigned constituted reciprocal gradients in the two parameters. That is, the adipose tissue had the highest S_{O_2} (1.0, or 100% oxygenated) and the lowest V_b (0.025), while the "tumor," when present, had the lowest S_{O_2} (0.5) and the highest V_b (0.1). Intermediate values were assigned to the parenchymal tissue. Because vascular dynamics will occur throughout tissue, we have modeled it by introducing sinusoidally time-varying behavior in V_b levels for each of the assigned tissue types. The amplitude of these variations was 10% of the mean value. The gradient in frequency was parenchyma > adipose > tumor. For the purposes of this demonstration, we did not include in the model variation of modulation frequency, phase, or depth of modulation *within* any tissue type.

The specific numerical values recorded in Table 1 for V_b and S_{O_2} are intended simply to accord with well-established qualitative trends that are seen in the hemodynamic properties of various tissue types, and as such are chosen somewhat arbitrarily. Thus, since it is known that white adipose tissue is relatively avascular and has a relatively low aerobic respiration rate,[17] it was assigned the lowest V_b and highest S_{O_2}. At the other extreme are the hemodynamic properties of the included tumor. Because enhanced angiogenesis is frequently found in breast tumors[18] and flow through many tumor types is sluggish relative to that of normal tissue,[19] we have assigned to this tissue the highest V_b and lowest S_{O_2}.

The scattering coefficient μ_s also varied among tissue types in the model medium. The gradient in μ_s was tumor > parenchyma > adipose. The specific values listed in Table 2 were chosen on the basis of recent estimates of optical coefficient values for the indicated tissues.[20] It was also assumed that the scattering properties and the oxygen saturation levels of the breast were time invariant.

For the purpose of computing photon-intensity distributions in the tissue model, it is necessary to derive an absorption coefficient μ_a for each tissue type from its V_b and S_{O_2} values. The manner in which this was accomplished is described in the Subsection 2.A.2.

2. Data Collection

The two-dimensional solver module of DANTSYS (diffusion accelerated neutral particle transport code system) was used to compute detector readings for the modeled breast map.[21] For computational convenience, the medium that was actually modeled in these calculations was a square with 8-cm edges and partitioned into 129×129 equal-area square fine mesh cells. The anatomical model shown in Fig. 1 was overlaid on this grid, and each fine mesh cell had assigned to it the optical properties of whichever tissue type occupied the majority of its area. Fine mesh cells in the "corner" regions between the circle and square were assigned the properties $\mu_a = \mu_s = 5\ \mathrm{cm}^{-1}$. This absorption is sufficiently strong that there is negligible reentry of light that exits from the circle. Vacuum boundary conditions, the physical equivalent of a Dirichlet mathematical boundary condition, were imposed at the edges of the square. The simulated measurement configuration consisted of a total of 18 detectors positioned a distance $1/\mu_s$ from the interior circular boundary and spaced at 20° intervals about the circumference, for each of six source positions that were spaced at 60° intervals. In all computations the refractive index was spatially homogeneous within the medium, and there was no index mismatch at the boundary. Under these conditions, the solution to the steady-state diffusion equation is not a function of the medium's refractive index. Therefore it was not necessary to assign an explicit numerical value to the medium's refractive index.

Detection of the time-varying hemodynamic states of the target media was achieved by simulating a two-wavelength measurement, at 760 nm and 840 nm. An idealized model of light-tissue interaction was employed, in that (1) it was assumed that oxygenated (oxy) and deoxygenated, or reduced (red), Hb are the only absorbing species present in the target media and (2) the absorption coefficients for whole blood were estimated by linear extrapolation of data obtained from dilute solutions of purified Hb (i.e., effects of concentration, scattering, other solutes, etc., were ignored). Consequently, the absorption coefficient computed for a given tissue type [see Eq. (1) below] is a simple linear combination of the μ_as of $\mathrm{Hb}_{\mathrm{oxy}}$ and $\mathrm{Hb}_{\mathrm{red}}$. In said linear combination, μ_a is weighted by the fraction of overall tissue volume that consists of blood (i.e., V_b) and by the fraction of all Hb that is in each state (i.e., S_{O_2} for $\mathrm{Hb}_{\mathrm{oxy}}$, $1 - S_{O_2}$ for $\mathrm{Hb}_{\mathrm{red}}$).

Numerical values for the monomeric millimolar extinction coefficients for both states of Hb (dimensions are $\mathrm{cm}^{-1}\ \mathrm{mM}^{-1}$) at these two wavelengths were obtained from the spectrophotometry literature.[22] The whole-blood molar absorption coefficient $\mu_{a_x}^{\lambda}$ at wavelength

Table 2. Mean Values of the Absorption and Scattering Coefficients Assigned to Each Tissue Type in the Dynamic Simulations

Tissue Type	μ_a, cm^{-1} 760 nm[a]	μ_a, cm^{-1} 840 nm[a]	μ_s, cm^{-1}
Adipose tissue	0.0349	0.0605	7.0
Parenchymal tissue	0.0580	0.0827	10.0
Tumor	0.2700	0.2140	15.0

[a] Numerical values reported here are derived from the assigned blood volume and oxygen saturation listed in Table 1, through formulas presented in Section 2.

λ for tetrameric Hb in oxygenation state x is related to the corresponding extinction coefficient ϵ_x^λ by $\mu_{a_x}^\lambda = 4000\, c\, \epsilon_x^\lambda / M$, where M is the molecular weight of Hb and c is its concentration. The numerical values assigned to these latter quantities were $M = 64{,}500\ \mathrm{g\,mol^{-1}}$ and $c = 150\ \mathrm{g\,L^{-1}}$. Mean tissue absorption coefficients ($\mathrm{cm^{-1}}$) were subsequently computed for each tissue type at each wavelength via the formula

$$\mu_{a_{\mathrm{tis}}}^\lambda = V_b[S_{\mathrm{O}_2}\mu_{a_{\mathrm{ox}}}^\lambda + (1 - S_{\mathrm{O}_2})\mu_{a_{\mathrm{red}}}^\lambda]. \quad (1)$$

The numerical values derived for the three tissue types, at both wavelengths, are reported in Table 2.

Two simulation experiments were conducted, with the target media differing only by the presence or absence of the included "tumor." In practice, this also could be interpreted as measurements made before and after administration of a dye. In each experiment, detector readings were computed at intervals of 0.5 s in the modulation cycle. The three tissue frequencies reported in Table 1 are multiples of 0.02 Hz; further, the adipose and parenchyma frequencies are multiples of 0.04 Hz. The fundamental modulation periods for the media with the tumor present and absent thus were 50 s and 25 s, respectively. Accordingly, 100 sets of detector readings were computed for the former medium, and 50 for the latter. Consequently the resolution bandwidth for each medium was the same as its fundamental modulation frequency, while the Nyquist frequency was 1.0 Hz in both cases.

For each modeled wavelength, an additional set of detector readings was computed from a homogeneous medium having the same size, geometry, etc. as the target media, and with $\mu_{s_{\mathrm{ref}}}^\lambda = \mu_{s_{\mathrm{adi}}}^\lambda$, $\mu_{a_{\mathrm{ref}}}^\lambda = \langle \mu_{a_{\mathrm{adi}}}^\lambda \rangle$ (ref, adi, and $\langle\,\rangle$ denote the reference medium, adipose tissue, and the mean value, respectively). We refer to this data set as the "detector-reference medium" (DRM) result. For each target medium and every source–detector pair (indexed by i) these reference values $(\mathbf{r}_{\mathrm{DRM}})_i$ and the "instantaneous" detector readings $r_i(t)$ computed were processed according to the function $[\Delta\mathbf{d}(t)]_i = [r_i(t) - (\mathbf{r}_{\mathrm{DRM}})_i]/(\mathbf{r}_{\mathrm{DRM}})_i$ to produce the *relative detector reading changes* that were subsequently supplied to the image reconstruction code as input (see Subsection 2.B.1 below). Note that the temporal mean value $\overline{r_i}$ for each detector could have been employed as an alternative to this sort of homogeneous fixed DRM, as is illustrated for the experimental data and as we apply in practice.[13–16] The time-series analysis results obtained are not qualitatively affected by the choice of DRM, and it is only for space-limitation reasons that simulation-study results obtained with only one type are presented below.

B. Laboratory Phantom Studies

1. Target Properties

All experiments were performed using a machined cup-like vessel composed of white Delrin as the target. The vessel had an external diameter of 7.6 cm, an internal free-space diameter of 7.3 cm, and a height of 15 cm. Intralipid at a concentration of 2% v/v (i.e., a fivefold dilution of the 10% stock solution) was added to form the background scattering medium; our estimates for the background optical coefficients are $\mu_s' \approx 20\ \mathrm{cm^{-1}}$ (Refs. 23–25), $\mu_a \approx 0.02\ \mathrm{cm^{-1}}$ (Ref. 26). The vessel was filled to within 0.5 cm of the top with 500 mL of the background medium. Suspended in the vessel was an apparatus supporting up to four latex balloons positioned within a cruciform frame. The balloons' positions in the frame are shown schematically in Fig. 2(a), and in a cross-sectional sketch in Fig. 2(b). Figure 2(c) is a sketch of the positions of the optical fibers about the vessel, i.e., the data collection geometry. Each balloon was filled with approximately 3 mL of 50-μM hemoglobin. Positioned above each balloon was a 5-mL syringe serving as a reservoir. Periodic variations in balloon volume were achieved by pneumatic displacement, causing a maximum volume change of approximately 1 mL. Several different experiments of this sort have been performed, of which we show only one here. The locations and dynamic properties of the balloons are shown schematically in Fig. 3. Four balloons were present, two of which were modulated at ~0.12 Hz, while the other two were stationary. In addition, the two modulated balloons were beating either in phase or 180° out of phase with each other.

2. Data Collection

Experimental data were collected using a recently described CCD-based fast imager with an iris-type measuring head.[12,27] Time-varying data were collected at a rate of 2 Hz, using a 6×6 binning factor (i.e., each detector reading was the sum of the signals arising from each of 36 contiguous CCD pixels). The average intensity for each spot {i.e., $[\mathbf{r}(t)]_i$} was then computed, by using a thresholding algorithm. Two distinct sets of normalized detector readings were derived from the resultant data: In one case the $[\mathbf{r}(t)]_i$ were normalized to the mean value obtained for each detector during the time-series acquisition [i.e., $(\mathbf{r}_{\mathrm{DRM}})_i = \overline{r_i}$]; in the other, to the signal obtained from the background medium in absence of the balloons and frame. Each of these sets of normalized values was subsequently used as the input data for image recovery. For the reported studies, a total of six multiplexed source positions, spaced at 60° intervals, were used to acquire the tomographic data. The illuminating wavelength was 810 nm, its intensity was approximately 2 mW, and the signal integration time was 10 ms. One hundred twenty sets of detector readings were collected in each experiment (60 s total acquisition time per source). Thus the Nyquist frequency was 1.0 Hz and the resolution bandwidth was 16.7 mHz.

C. Image Reconstruction

Images of the absorption coefficient, μ_a, and diffusion coefficient D, with $D = [3(\mu_a + \mu_s)]^{-1}$, at each of the modeled illumination wavelengths, were simultaneously recovered through use of a previously described finite-element (FEM)-based software package for optical tomography.[28] This employs a conjugate-gradient-descent (CGD) algorithm to compute the solution to a linearized perturbation equation (i.e., first-order Born approximation) in each element of an FEM mesh. Reconstructions terminated when a preset convergence threshold was met or after 2000 CGD iterations, whichever came first. The Jacobian operator and reference detector readings were computed from numerical solutions

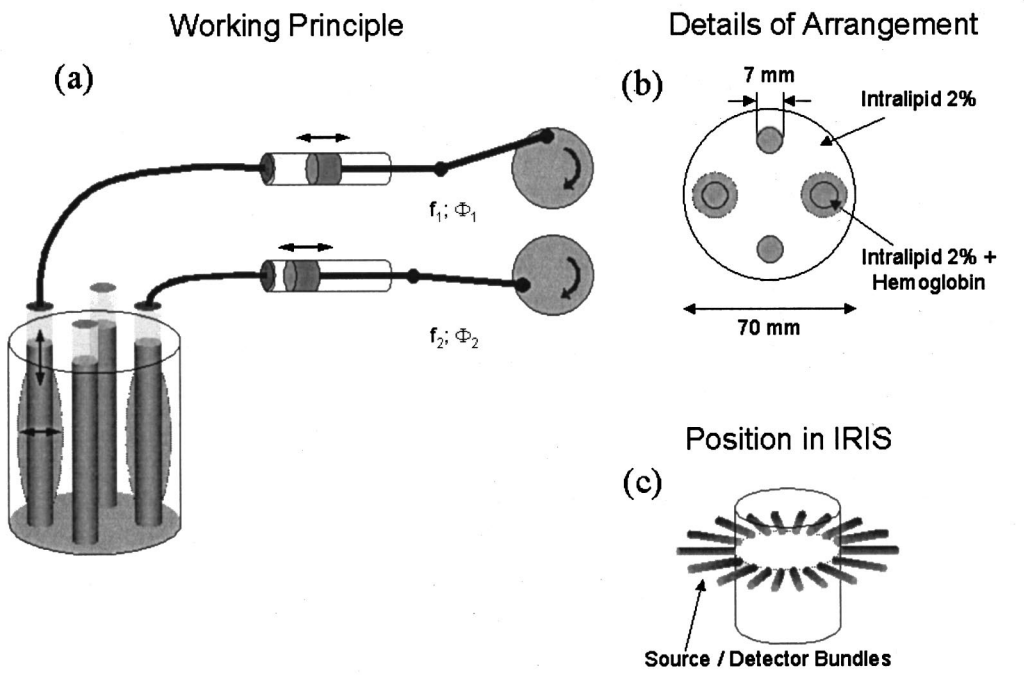

Fig. 2. Sketch of the essential components of the apparatus used for the laboratory phantom experiments, showing (a) the mechanism used to rhythmically inflate two balloons, (b) the position of the latex balloons in the cylinder, and (c) the geometric arrangement of optical fibers about the cylinder.

of the photon diffusion equation, with extended Dirichlet boundary conditions, for a homogeneous reference medium that we refer to as the "image-reference medium" (IRM). The symbols used here for the operator and reference detector readings are $\mathbf{W}_{\mathrm{IRM}}$ and $\mathbf{r}_{\mathrm{IRM}}$, respectively. The vector $\mathbf{r}_{\mathrm{IRM}}$ has as many elements as there are detector readings associated with each time point (108 for the examples presented here). $\mathbf{W}_{\mathrm{IRM}}$ is a matrix with the same number of rows that $\mathbf{r}_{\mathrm{IRM}}$ has, while the number of columns is equal to the product of the number of elements in the FEM mesh (i.e., 1536) and the number of optical coefficients being solved for in each element (i.e., 2).

The time-dependent vector of relative changes in detector readings [$\Delta\mathbf{d}(t)$, which was defined in Subsection 2.A.2 above] is transformed into a set of perturbations of the detector readings computed for the IRM, $\Delta\mathbf{r}'(t)$, by $[\Delta\mathbf{r}'(t)]_i = [\Delta\mathbf{d}(t)]_i(\mathbf{r}_{\mathrm{IRM}})_i$. (That is to say, $\Delta\mathbf{r}'(t)$ is a composite of *three* distinct detector readings: those from the target medium, the DRM, and the IRM.) The image reconstruction algorithm computes a solution to a modified perturbation equation $\Delta\mathbf{r}'(t) = \mathbf{W}_{\mathrm{IRM}}\Delta\mathbf{x}'(t)$. While $\Delta\mathbf{x}'(t)$ is not identical to the vector of perturbations in the optical coefficients relative to the IRM, extensive trial studies have shown that the image recovered has strong positive spatial correlations with the true coefficient distributions for IRMs having properties sufficiently different from those of the target medium that comparably good results could *not* be obtained by using a conventional perturbation formulation.[28]

1. Simulation Studies

The size and shape of the IRM chosen for analysis of these sets of detector readings were the same as those of the target media, while its optical properties were $\mu_{s_{\mathrm{ref}}}^{\lambda} = \mu_{s_{\mathrm{adi}}}^{\lambda}$, $\mu_{a_{\mathrm{ref}}}^{\lambda} = \langle \mu_{a_{\mathrm{adi}}}^{\lambda} \rangle$ (i.e., for this demonstration, the properties of the IRM are identical to those of the DRM, although this is *not* a requirement for successful image reconstruction[28]; it also is *not* essential that the IRM be homogeneous).

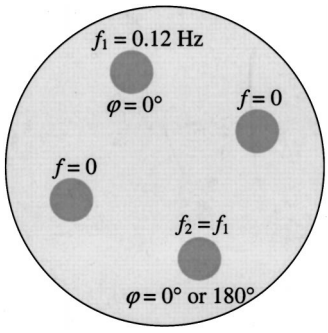

Fig. 3. Sketch showing the details of the arrangement of latex balloons in the two laboratory phantom experiments, and the frequencies and (where applicable) relative phases of the pulsating balloons.

For the purposes of the present report, the detector readings were evaluated in the absence of added noise. In other studies we have modeled more complex states and time-varying functions.[13–16,28] This includes the limiting case of spatiotemporal coincident behavior involving either simultaneous variations in μ_a and D according to different functions (e.g., quasiperiodic, chaotic, or stochastic time series)[29] or to simultaneous variations in V_b and S_{O_2} (Ref. 30).

The formulas used to compute estimates of V_b and S_{O_2} from the reconstructed values of $\mu_{a_{\mathrm{tis}}}^{760}$ and $\mu_{a_{\mathrm{tis}}}^{840}$ are easily

derived by writing Eq. (1) for $\lambda = 760\,\mathrm{nm}$ and for $\lambda = 840\,\mathrm{nm}$ and then solving for the hemodynamic parameters in terms of the optical coefficients. When this is done, the result is

$$V_b = \frac{(\mu_{a_{\mathrm{red}}}^{840} - \mu_{a_{\mathrm{ox}}}^{840})\mu_{a_{\mathrm{tis}}}^{760} - (\mu_{a_{\mathrm{red}}}^{760} - \mu_{a_{\mathrm{ox}}}^{760})\mu_{a_{\mathrm{tis}}}^{840}}{\mu_{a_{\mathrm{red}}}^{840}\mu_{a_{\mathrm{ox}}}^{760} - \mu_{a_{\mathrm{red}}}^{760}\mu_{a_{\mathrm{ox}}}^{840}},$$

$$S_{\mathrm{O}_2} = \frac{\mu_{a_{\mathrm{red}}}^{840}\mu_{a_{\mathrm{tis}}}^{760} - \mu_{a_{\mathrm{red}}}^{760}\mu_{a_{\mathrm{tis}}}^{840}}{(\mu_{a_{\mathrm{red}}}^{840} - \mu_{a_{\mathrm{ox}}}^{840})\mu_{a_{\mathrm{tis}}}^{760} - (\mu_{a_{\mathrm{red}}}^{760} - \mu_{a_{\mathrm{ox}}}^{760})\mu_{a_{\mathrm{tis}}}^{840}}. \quad (2)$$

Values for the hemodynamic coefficients were calculated, by means of Eq. (2), in each pixel and at each value of the time index.

The reconstructed images of the diffusion coefficients D^{760} and D^{840} were not combined in any way; the image time series for each wavelength was analyzed separately.

2. Laboratory Phantom Studies

Images were recovered by using the same reconstruction algorithm as for the simulation studies. The IRM selected for analysis of these data sets was homogeneous, and its properties were $\mu_a = 0.02\,\mathrm{cm}^{-1}$, $\mu_s = 15\,\mathrm{cm}^{-1}$, and a diameter of 8.0 cm. Because only one source illumination wavelength was employed, estimation of the phantoms' V_b or S_{O_2} could not be attempted. Typically, a total of 120 images (30 s physical time for data acquisition) were obtained for each source position. Tikhonov (ridge) regularization was used to minimize the amplitude of artifacts; it was found empirically that 1×10^{-6} was an effective value for the regularization parameter. Apart from this, no image enhancement scheme or update procedure was used.

3. Note Regarding Preparation of Contour Maps

The FEM mesh that was used for all inverse computations computed D and μ_a values in 1536 irregularly spaced triangular finite elements, all of which lie within the circular boundary shown in Fig. 1. In preparing the contour maps presented below in Results, this mesh was converted to a 40×40 square grid by employing a linear interpolation algorithm[31] based on a Delaunay triangularization[32] of the FEM mesh. One of the considerations that went into the selection of the rectangular grid size was minimizing the reduction in spatial resolution that inevitably would result from these operations. In the contour maps that were finally produced, significant artifacts appear only in the vicinity of the circular boundaries of the target media (see, e.g., Fig. 10 below), and even these are not prominent in every case.

D. Time-Series Analysis of Detector Readings and Images

Where indicated, standard time-series analysis methods[33,34] were used to compute the frequency and time-correlation response of the detector or image data. The analysis included computation of cross-correlation and its spectral components, the cross-spectral density and coherence functions. An elementary FORTRAN code was used to compute the target-versus-image correlations, while library functions in the signal analysis toolbox of MATLAB 5.2, Release 10 (The Mathworks, Inc., Natick, MA) were employed for all other time-series analysis computations. A brief description of these functions follows.

Consider two time-varying functions $u(t)$ and $v(t)$ that are sampled at a set of discrete times t_n, where $n = 1,\ldots,N$ and $t_n - t_{n-1} = \Delta t$ is a constant. (All formulas that follow can be adapted to the case of nonconstant time intervals, but this was not necessary for analysis of data considered in this report.) Then we define

$$u_n \equiv \begin{cases} u(t_n), & n = 1,\ldots,N \\ 0, & n < 1 \ \text{ or } \ n > N \end{cases},$$

$$v_n \equiv \begin{cases} v(t_n), & n = 1,\ldots,N \\ 0, & n < 1 \ \text{ or } \ n > N \end{cases},$$

and use the symbols $\bar{u}$ and $\bar{v}$ to denote the mean values of these two discrete time series, and s_u and s_v for their standard deviations.

For each N-point time series u_n and v_n, the MATLAB "fft(x)" function[35] was used to compute the discrete Fourier transforms (DFTs)

$$U_k^R + jU_k^I = \sum_{n=1}^{N} u_n \exp[-j(2kn\pi/N)],$$

$$V_k^R + jV_k^I = \sum_{n=1}^{N} v_n \exp[-j(2kn\pi/N)], \quad (3)$$

where $j = \sqrt{-1}$, the superscripts R and I denote the real and imaginary parts, respectively, of the DFT, and the subscript k is the frequency-component index ($k = 0,1,\ldots,N/2$ for N even; $0,1,\ldots,(N-1)/2$ for N odd).

The formal definition employed for the cross correlation (cc) between the two time series is

$$cc_{uv}(m) \equiv \frac{1}{(N-1)s_u s_v} \sum_{n=1}^{N} (u_n - \bar{u})(v_{n+m} - \bar{v}), \quad (4)$$

where the parameter m is called either the "delay" or the "lag." It should be noted here that different authors use different definitions for cross correlation. In this report the definition of Jenkins and Watts[34] is used, in that Eq. (4) entails subtraction off of the mean values and division by the product $(N-1)s_u s_v$ to produce a dimensionless quantity whose absolute value is $\leqslant 1$. This convention is not universal—Bendat and Piersol,[33] for example, define cross correlation as the *un*normalized function $R_{uv}(m) \equiv \Sigma_{n=1}^{N} u_n v_{n+m}$, and refer to the quantity defined in Eq. (4) as the "correlation coefficient function"—but is appropriate for our purposes. We have the capability to calculate cross correlations either between the time series of reconstructed images in *two* image pixels, or between the image series in *one* pixel and any one detector-readings time series. Subsequent to appropriate preprocessing of the input time series, the Matlab "xcorr(x,y,'option')" function,[36] with "option" set to "coeff," is used to perform these computations.

The cross-spectral density (CSD) function G_{uv} of the time-series pair u and v is the Fourier transform of their

cross-correlation function.[33,34] It is preferable in practice to compute G_{uv} directly from the DFTs U and V. Operationally, the full N time-point time series u and v are first subdivided into some number n_d of "records," with N/n_d time points per record. (The "correct" value for n_d is application-dependent, and choosing it is an art.[37] Increasing n_d leads to more accurate coherence ($v.i.$) estimates, but at the cost of increased resolution bandwidth.) A DFT computation—$U(n)$, $V(n)$, $n = 1,2,\ldots,n_d$—is carried out for each record, and the cross-spectral density estimate is

$$G_{uv}(k') = \frac{2}{N}\sum_{n=1}^{n_d}[U^R_{k'}(n) - jU^I_{k'}(n)][V^R_{k'}(n) + jV^I_{k'}(n)], \tag{5}$$

with $k' = 0, 1, \ldots, N/(2n_d)$ for N even; $0, 1, \ldots, (N-1)/(2n_d)$ for N odd. Just as for the DFTs, the real and imaginary parts of the CSD are converted to amplitude and phase for display purposes. Apart from the value that it has in itself, the result of the CSD computation is then used to compute the coherence γ^2_{uv} between u and v, via the formula

$$\gamma^2_{uv}(k') = \frac{G_{uv}(k') \cdot G^*_{uv}(k')}{G_{uu}(k') \cdot G_{vv}(k')}. \tag{6}$$

The asterisk superscript in Eq. (6) denotes the complex conjugate, and the quantities in the denominator are the *auto*spectral densities of u and v. The latter are identical to the power spectra of u and v. It is apparent from the form of Eq. (6) that γ^2_{uv} is dimensionless; proof that, in addition, $0 \leqslant \gamma^2_{uv} \leqslant 1$ is straightforward.[33] Our spectral density and coherence computations are performed by use of, after appropriate preprocessing of the input time series, the Matlab functions "csd(x,y,nfft,fs,'dflag')"[38] and "cohere(x,y,nfft,fs,'dflag')."[39] For the examples presented in Results, the "dflag" parameter was set to "none."

While the value of cc_{uv} for a given time lag takes into account the impact of all frequencies simultaneously, G_{uv} and γ^2_{uv} contain a wealth of frequency-dependent information regarding the manner in which the two time series u and v are or are not related. Peaks in the amplitude of G_{uv} indicate those frequencies at which there is appreciable power in *both* u and v, while the phase shows, at each frequency, whether u leads or lags v, and by how much.[34] There are several equivalent interpretations for γ^2_{uv}: It is analogous to a frequency-dependent correlation coefficient[34]; it is a measure of the fraction of the total power in v that is due to linear contributions from u, at each frequency[33]; it is an estimate of the probability, at each frequency, that both u and v are responses to a common cause; it is a measure of the degree to which the phase difference between u and v at the beginning of the measurement period persists throughout the duration of the period (the closer γ^2_{uv} is to 0, the more rapidly the phase difference changes).[40]

Meaningful estimates of G_{uv} can be obtained with $n_d = 1$ in Eq. (5). However, $n_d > 1$ is a necessary condition for valid computation of γ^2_{uv} via Eq. (6); taking $n_d = 1$ leads to a meaningless result of $\gamma^2_{uv} = 1.0$ at all frequencies.[33] The standard errors of the computed estimates of G_{uv} and γ^2_{uv} are proportional to $n_d^{-1/2}$ (Ref. 33). Therefore when working with experimental or clinical data it is important to select a value for n_d that ensures that these errors are acceptably small. However, because the demonstrational studies reported on here are based on simulation data that is perfectly periodic and noise-free (G_{uv} and γ^2_{uv} results are not presented for the experimental data), there is no random error in the computed CSDs and coherences, and we used $n_d = 1$ for G_{uv} computations and $n_d = 2$ for γ^2_{uv} computations. Thus the coherence results presented below can be interpreted as a measure, at each frequency, of the extent to which the phase relationship between two time series is different in the first and second halves of the full observation period.

3. RESULTS

A. Simulation Studies

As indicated, a goal of this study was to test the hypothesis that the occurrence of dynamic behavior in optical coefficients can serve to aid in assessing the qualitative accuracy of reconstructed features present in complex backgrounds. To explore this we have computed a time series of image data from a segmented MR map of the breast to which we have assigned time-varying behavior in V_b to the various tissue types. This was accomplished by assigning the appropriate values for μ_a to the corresponding tissue types that would produce the desired dynamic behavior in V_b based on a two-wavelength measurement. The assigned hemodynamic and optical coefficients are listed in Tables 1 and 2, respectively.

Already cited is the concern regarding the low spatial resolution of images obtained from complex backgrounds. An example of such results is shown in Fig. 4. [It is worth noting that we have achieved, as have others,[41,42] improved image quality using more-intensive computational efforts (e.g., Newton-type updates). In practice, however, such efforts may have limited value owing to the computational burden they present. Besides, even with such efforts, we are unaware of any reports claiming good image quality from physiological measurements.] Panel (a) shows a contrast map of time-averaged V_b for the assigned target medium containing a centrally located included tumor. The upper limit of the plotted range in Fig. 5(a) is 0.05, even though $\langle V_b \rangle = 0.1$ in the tumor (see Table 1), only because of practical limitations associated with displaying these results in the form of a gray-scale map. Panel (b) shows the contrast map of the time-averaged reconstructed value for V_b. Comparison reveals elevated levels of V_b in the vicinity of the tumor and surrounding parenchyma. Significantly, while this feature is qualitatively correct, the presence of the tumor is by no means obvious. Panel (c) shows that a qualitatively different result is obtained from examination of the same target medium, but lacking the tumor. Individual images in each time series, furthermore, qualitatively closely resemble the mean images shown. This indicates that the low spatial resolution seen in the figures is not a blurring phenomenon due to dynamic behavior, but originates from the input data and reconstruction algorithm.

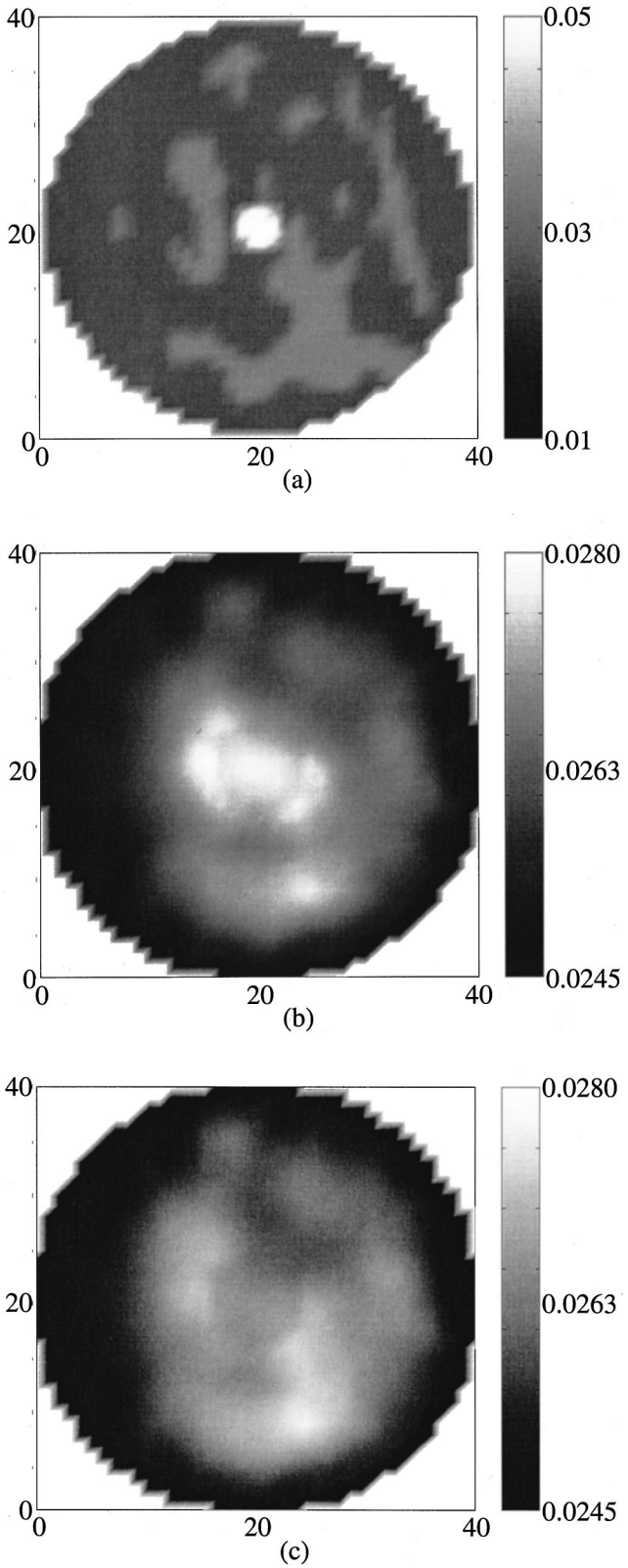

Fig. 4. (a) mean value, in each pixel, of V_b in the tumor-bearing target medium averaged over all 100 time points during which the absorption coefficients of the tissues were modulated. (b) and (c) $\langle V_b \rangle$ images of the tumor-bearing and tumor-free target, respectively.

The tumor's presence is clearly revealed by computing a difference image [Fig. 4(b) minus Fig. 4(c)], as shown in Fig. 5. Results (not shown) similar to those in Figs. 4(b) and 4(c) were obtained for images corresponding to S_{O_2}, D^{760}, or D^{840}. In practice, such differencing may be possible through the use of injectable dyes that are selectively retained by the vasculature associated with a tumor.[43] As this constitutes an invasive procedure, even if minimally so, the question of whether or not it is possible to identify the presence of the tumor from examination of data derived from *only* the medium containing the tumor retains its importance.

Results in Fig. 4(b) demonstrate that qualitatively accurate information (e.g., location and gradient in V_b) regarding the tumor is present in the image data, albeit mainly obscured by the low spatial resolution. In practice, further degradation of image quality can be expected from artifacts originating from noise and other uncertainties of measurement. As is, it seems doubtful that recovered image quality [Figs. 4(b) and 4(c)] would prove useful for most clinical applications. This leads to the question we are interested in examining: Given such uncertainties, can information specific to the tumor, that better reveals its presence, be derived from examination of a time series of image data? As indicated in Section 2, one notable feature we have incorporated into the dynamic simulation is the known sluggish state of perfusion in the vicinity of solid tumors. This was modeled by assigning a diminished S_{O_2}, elevated V_b, and reduced rate of rhythmic activity to the tumor. We note that the last, while perhaps not naturally occurring, could be imposed by a simple manipulation (e.g., rhythmic mild compression) of the tissue. Alternatively, the conditions considered could be taken as a crude model of the known structure-dependent frequency response of the vasculature, wherein the included object corresponds to some particular localized vasomotor activity that is either naturally occurring[44] or induced.

An indication that additional information regarding the modeled hemodynamic state is present in the recovered image time series is shown in Fig. 6, panels (a) and

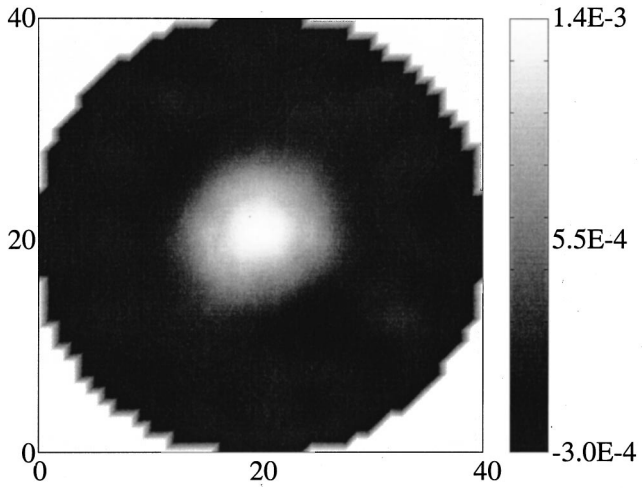

Fig. 5. Mean value of the differences between images of the tumor-bearing and tumor-free media, $\langle \Delta V_b \rangle$.

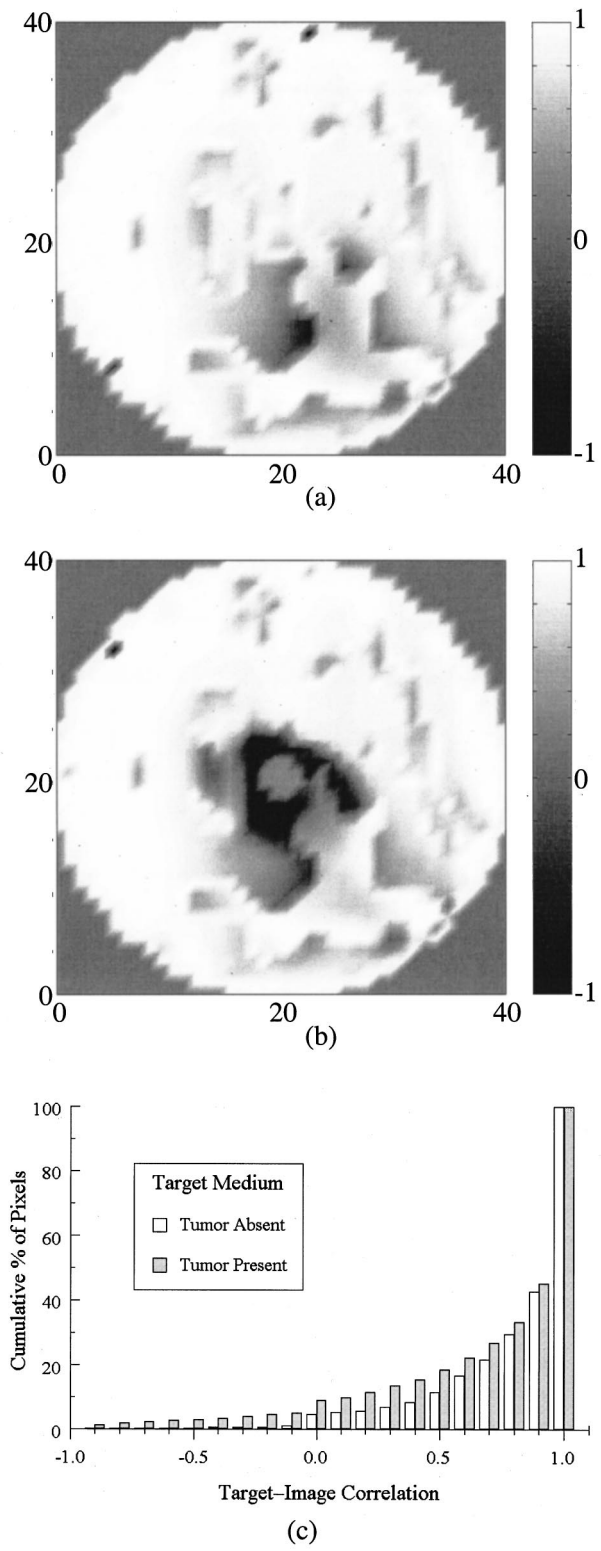

Fig. 6. Cross correlations, for zero time lag, between V_b time series of the target media and of the reconstructed images. (a) map of $cc_{uv}(0)$ for the tumor-free medium, where u is the target V_b and v is the image V_b; (b) analogous map, for the tumor-bearing medium; (c) bar graphs of the cumulative percentage of pixels for which $cc_{uv}(0)$ is between -1 and $(0.1n - 1)$, $n = 1,2,\ldots, 20$, for both media.

(b). These maps display the zero-time-lag cross-correlation, in every pixel, between the V_b time series in the target and reconstructed image series for tumor-free and tumor-containing media, respectively. Inspection reveals that the temporal variations between target and reconstructed images are positively correlated in almost all pixels [95.5% in Fig. 6(a), 91.1% in Fig. 6(b)] with a correlation value > 0.8 in the majority (70.1%, 66.5%). This implies a nearly linear relation, in these pixels, between the V_b in the target and those of the reconstructed images. The accompanying bar graph in Fig. 6(c) is a plot of the cumulative percentage of pixels for which the correlation is between -1 and $(i - 10)/10$, where $i = 1,2,\ldots, 20$. Inspection shows, quantitatively, just how few image pixels are uncorrelated or negatively correlated with their corresponding target medium pixels.

We note that there is an anomalous region in the lower right portion of Fig. 6(a), where several pixels have negative target/image correlations (the strongest negative correlation in any one pixel is -0.73). The phenomenon is even more striking in Fig. 6(b), wherein negative correlations, some approaching -1, are seen near the center and about the tumor. Careful comparison of these figures reveals that the negative correlations are restricted to regions where large variations in the medium's properties occur on a small spatial scale: the medium-air boundary, the reentrant border of the large parenchyma "island" in the lower right region, and the complex parenchyma–adipose–tumor–adipose–parenchyma–adipose transition in the center. The same behavior was seen in the maps of target/image diffusion-coefficient correlation (not shown) as well, with an even more pronounced tendency toward negative correlations in pixels near the medium-air boundary. While a complete accounting of this phenomenon is lacking, we believe that it simply is a consequence of limited spatial frequency content of the FEM mesh used. Use of a finer mesh presumably would yield even better temporal results.

Upon first consideration, it might seem that the results in Figs. 4 and 6 are irreconcilable. How can it be that the reconstructed time-series images are such crude representations of the target media and the very same images and target are so strongly positively correlated? The reason lies in the fact that correlation is insensitive to errors in scale. This can be grasped intuitively by considering a hypothetical image time series wherein every pixel is quantitatively inaccurate compared to the target, and the magnitude of the error differs in every pixel. In such a case, the individual images will not appear at all similar to the target. If, however, the relative error in each pixel is consistent throughout the time series, always underestimating or overestimating the true value of the optical or hemodynamic parameter by the same fraction, then the temporal variations in every pixel will be perfectly correlated with those of the target.

An implication of the preceding observations is that the application of well-established time-series analysis techniques to an optical image time series might well permit the extraction of dynamic features with an accuracy and spatial resolution superior to those obtained for the reconstructed optical or hemodynamic parameters *per se*. This expectation is borne out by results shown in Fig. 7. Here

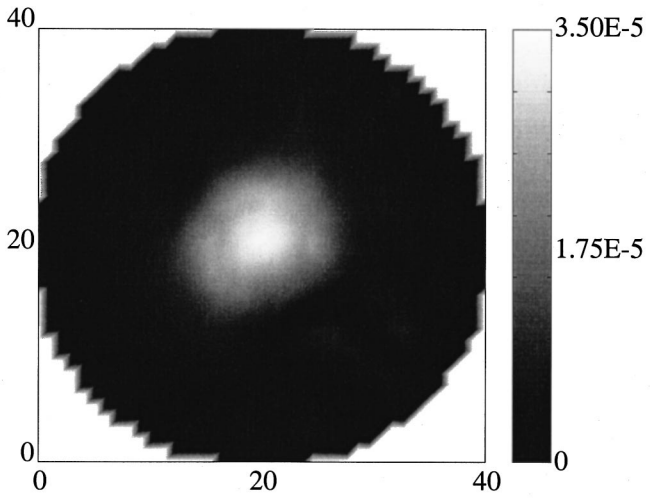

Fig. 7. DFT amplitude map of the V_b images of the tumor-bearing target medium. The frequency selected for display purposes is 0.06 Hz, which is the tumor modulation frequency.

we show a map of the amplitude of the DFT at the tumor modulation frequency (0.06 Hz), computed from the complete time series of 100 images of V_b. Significantly, comparison of this map with the difference image shown in Fig. 5 reveals the two results are qualitatively nearly identical. The critical difference here, however, is that correct identification of the tumor's presence was revealed without resorting to any artificial differencing methods. Rather, its presence is revealed from analysis of *only* the tumor-containing medium's image time series.

The preceding observation has led to further considerations. For instance, it is well appreciated that any difference between two time series, irrespective of the physical origin, may serve to distinguish them. When applied to the image, this indicates that time-varying behavior associated with different regions might be distinguished just as well or even better, thereby improving spatial contrast, by the *absence* of temporal features in a particular region. Accordingly, we have examined the image time series' frequency-dependent DFT amplitude maps and paid close attention to the "mixing frequencies," which are the sums and differences between any two of the modulation frequencies assigned to the individual tissue types. Presented in Fig. 8 is a particular frequency component (amplitude and phase map) of the DFT of the V_b time series. The selected frequency, $f = 0.52$ Hz, is a mixing frequency equal to the sum of the parenchyma and adipose modulation frequencies (see Table 1). Inspection shows that the presence of tumor is clearly revealed in both the amplitude and phase maps. Specifically, the greatly reduced 0.52-Hz amplitude in the center of Fig. 8(a) reveals the presence of the tumor, as does the existence of a localized, well-defined central region of negative phase within the otherwise mainly positive phase map in Fig. 8(b). It should be pointed out that the displayed phase range was restricted to $-90°$–$+90°$ solely because of practical limitations associated with plotting these results in the form of a gray-scale map. When the same data are displayed as a colored map, the large ($\sim$100°) phase difference between the regions corresponding to the tumor and healthy tissues is easily seen, even if the full $-180°$ to $+180°$ range is included.

Significantly, the feature contrast in Fig. 8 is on the order of one hundred times that revealed in the optical contrast maps. Note also that the size, shape, and sharpness of the edge detected for the tumor are superior to those seen in the mean-difference image (Fig. 5) or the tumor-frequency DFT amplitude (Fig. 7) and are comparable to those of the "ideal" target [Fig. 4(a)].

While striking, the result shown in Fig. 8 considers a signal whose amplitude frequently is low (i.e., a mixing frequency). It would be better to produce a map that is equivalent in terms of its contrast level but that makes use of a large-amplitude signal. This criterion does not by itself limit which of the many time-series functions could be applied. A useful consideration in the context of investigating hemodynamic states is the previously cited structure-dependent frequency response of the vascula-

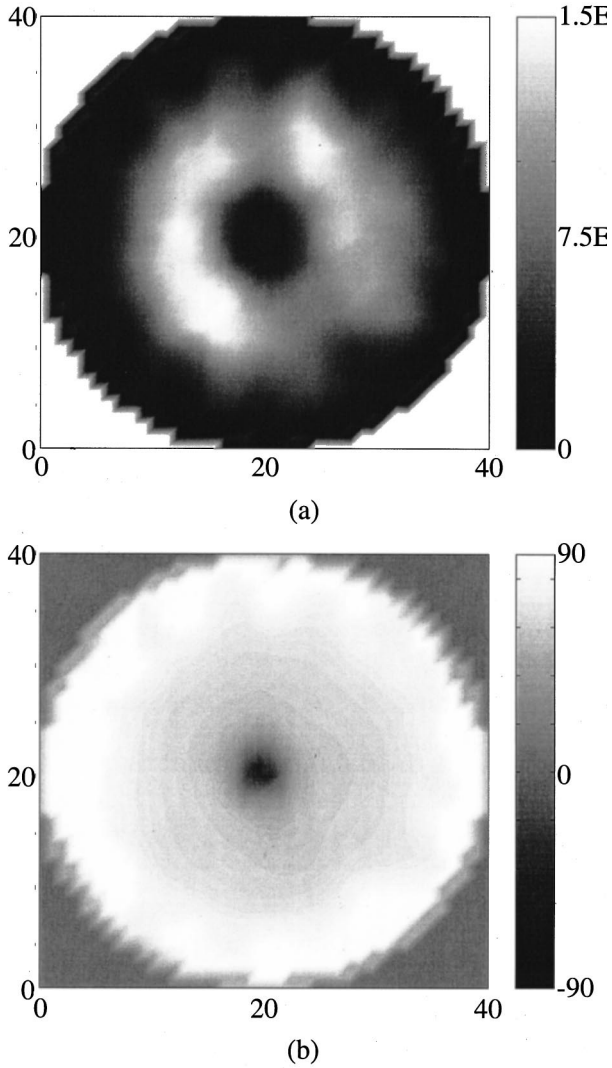

Fig. 8. DFTs of the V_b images of the tumor-bearing target medium. In both panels the frequency selected for display purposes is 0.52 Hz, which is the sum of the modulation frequencies of the adipose and parenchyma tissues. (a) DFT amplitude; (b) DFT phase.

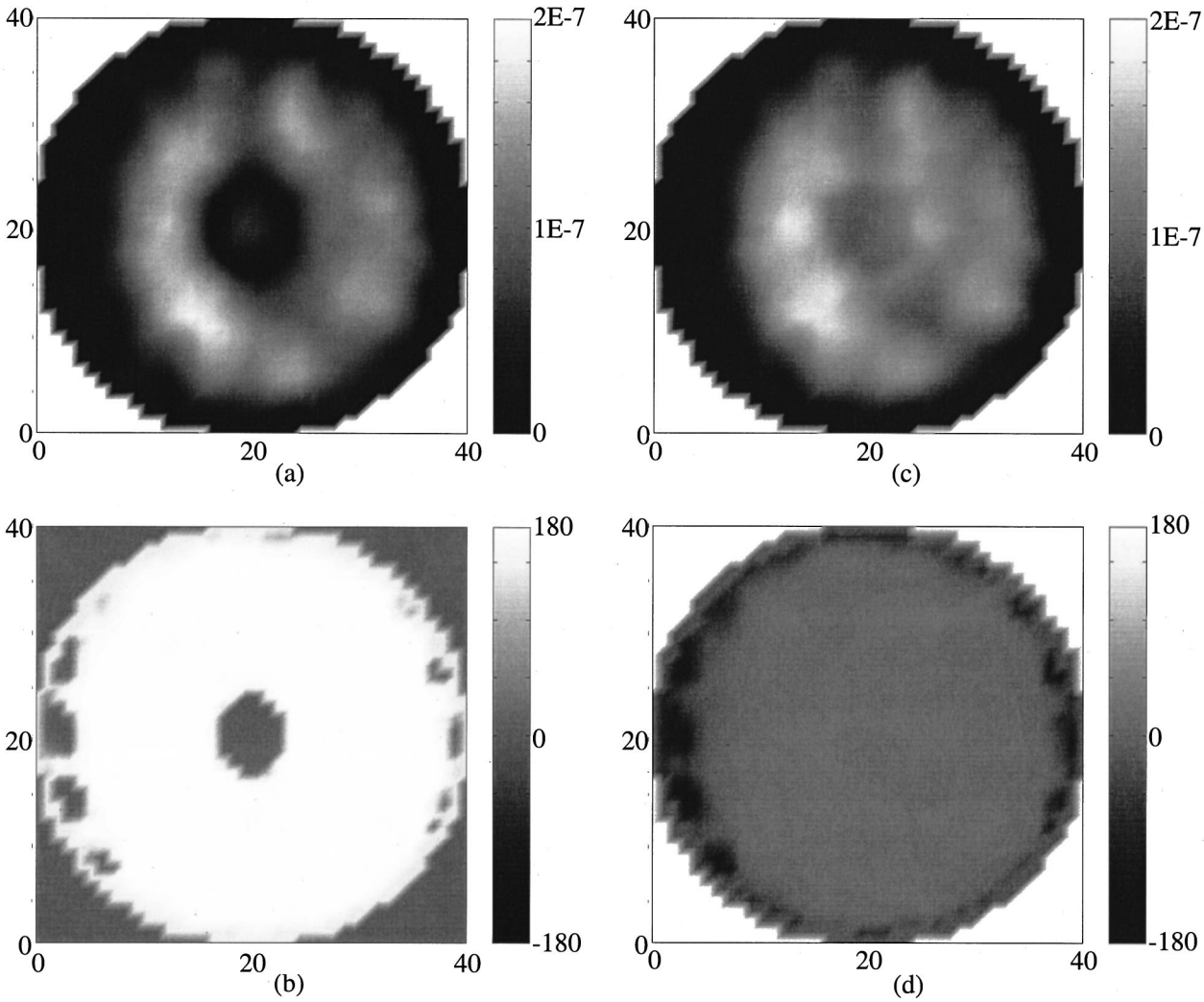

Fig. 9. Maps of cross-spectral density between the temporal trend in a particular "index pixel" and those of all pixels in the target medium, for the V_b images. For all results shown here, index pixel is at coordinates (20,20) (i.e., center of image), and the frequency component displayed is $f = 0.52$ Hz (i.e., sum of adipose and parenchyma modulation frequencies). (a) amplitude, target with tumor; (b) phase, target with tumor; (c) amplitude, target without tumor; (d) phase, target without tumor.

ture. For instance, it is clear that tissue perfusion is, in some manner, a coordinated response. Certainly there are many disease processes that might interfere with such activity, and knowledge of the spatial locations of such anomalous regions would be useful. Such relationships are well revealed by a cross-spectral density analysis. For example, it is known that the respiratory rhythms of the vasculature, observed within many tissues, do not arise locally but result from central mechanisms that are common to all points within the image field. It would therefore be expected that the interpixel CSD would have a large amplitude at that frequency, for any two pixels, and that its phase would be largely independent of the duration of the measurement period or of the choice of the parameter n_d in Eq. (5). Failure of the CSD to meet either of these two expectations might serve as a signature for some pathological process.

Selected results of such an analysis performed on the image series are shown in Fig. 9. Panels (a) and (c) show the amplitude of the CSD between an index pixel located at the center of the image grid and all other pixels, for the tumor-containing and tumor-free media, respectively. As with other measures of temporal features, we observe that the tumor is clearly revealed when it is present and that the contrast between various regions is markedly reduced when it is absent. An even clearer identification of the presence or absence of the tumor can be seen in the phase maps [panels (b) and (d)]. Note the remarkable sharpness of the transition in phase that occurs within a short distance beyond the physical edge of the tumor. It is worth emphasizing that the selected pixel in no way biases the derived contrast maps. Choice of any other pixel in the image as the index will influence only the absolute values of the CSD amplitude or phase, and has *no* effect on the qualitative appearance of the map.

A similar, but perhaps even more impressive, result is shown in Fig. 10, where we present maps of the interpixel coherence functions between the index pixel (row 11, column 13) and all other pixels in the images of V_b. In order to attain the two objectives of decreasing the reso-

lution bandwidth (which, because $n_d = 2$ when computing coherences, is twice that obtained in the DFT and CSD computations) and generating coherence functions that have the same frequency components for both media, we worked with the periodic extension of each image time series [i.e., $V_b(n + 100) = V_b(n)$ for the tumor-containing medium, $V_b(n + 50) = V_b(n)$ for the tumor-free medium], with each one's length set to $N = 105$ time points. This is a justifiable artifice because in this way we model real-world conditions (such as were encountered in collecting the experimental data), in which the frequency structure of the medium is not known *a priori* and the length of the measurement time series essentially is arbitrary. The particular results shown in the figure are the $f = 0.54$ Hz (which is, for numerical reasons, as close as we can come to the sum frequency of the adipose and parenchyma tissues in this calculation) component of the computed coherence of the image time series for each target medium. The result for the tumor-containing medium is shown in panel (a). It is seen that the index pixel is strongly coherent with all other pixels *except* those adjacent to the exterior boundary or in the region where the tumor lies, while its coherence with pixels in the latter area is close to zero. In fact, the size, location, and shape of the tumor are almost perfectly recovered. In the corresponding result for the tumor-free medium, shown in panel (b), the index pixel is strongly coherent with almost all the other pixels. In addition, these results directly demonstrate that detection, location, and sizing of the tumor, if it is present, can be accomplished without any prior knowledge of its presence or whereabouts. In Subsection 3.B we present experimental results confirming the ability to image dynamic features in dense scattering media.

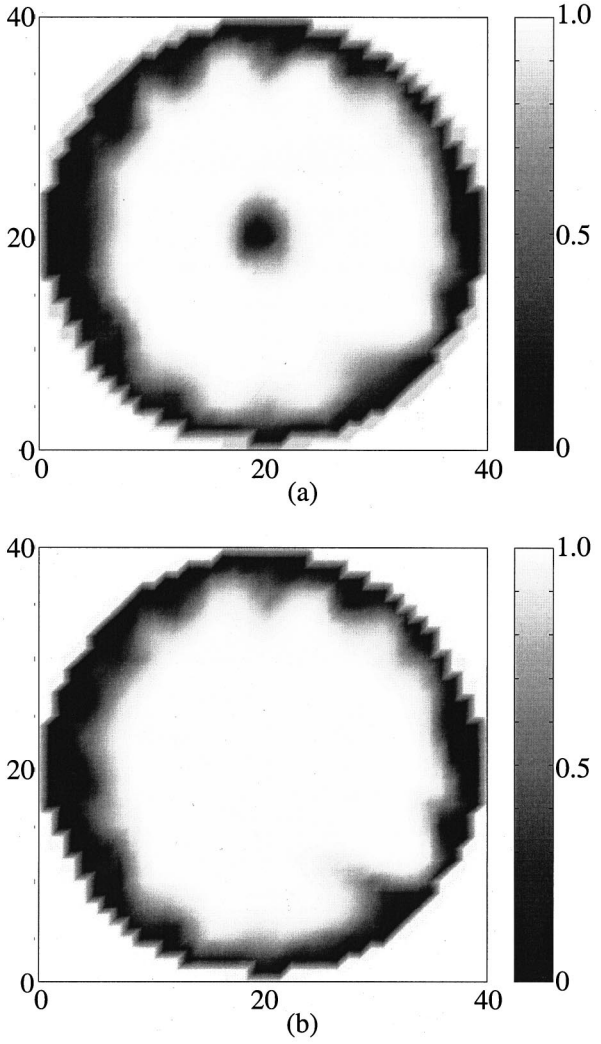

Fig. 10. Selected frequency component of the coherence functions computed by comparison of the temporal trend in a particular "index pixel" and those of all pixels in the target medium, for the V_b images. All results shown here are for frequency of 0.54 Hz. (a) target medium contains tumor, index pixel is row 11, column 13 (i.e., outside tumor); (b) target medium without tumor, index pixel is row 11, column 13.

B. Laboratory Phantom Studies

Four balloons were present in the experiment, two of which were static while the other two were modulated at a fixed frequency, with a relative phase of either 0° or 180°. An example of the reconstructed absorption image obtained at a single time point is shown in Fig. 11, panel (a). Four objects clearly are present, but they are not well resolved and their true diameters are not accurately recovered. The DFT amplitude at the 0.12-Hz modulation frequency is seen in panel (b). Shown is the fact that only two of the balloons are modulated at this frequency. Also evident is that the spatial resolution of the DFT map is considerably improved compared with the map shown in panel (a). The phase portions of the DFTs at 0.12 Hz for the in-phase and the 180°-out-of-phase cases are shown in panels (c) and (d), respectively. The correct phase relation between the two modulated balloons is recovered in each case. [Amplitude, panel (b), is shown for only the latter case, because, as expected, the corresponding map for the former is nearly identical.] In a similar experiment that has been reported elsewhere,[12] it was shown that the dynamic balloons could be distinguished on the basis of differences in frequency as successfully as they were here on the basis of differences in phase.

Also seen in Fig. 11, panels (c) and (d), are near-surface regions where the phase values are markedly different from those in the interior. Note that these occur in regions where the amplitude is nearly zero [cf. panel (b)].

4. DISCUSSION

A confounding feature of optical imaging studies of tissue is that the image quality can be sufficiently limited that it may be difficult to easily distinguish between artifact and true features recovered with low resolution. Compounding this is the fact that, owing to vascular reactivity, fluctuations in tissue blood volume can introduce considerable variability in the measured intensity levels. Thus, depending on how data are acquired, the repeatability of information derived from tissue studies could be limited. We recognize, however, that because the vasculature exhibits a structure-dependent frequency response, it should be possible to correlate measures of the temporal variability of the vascular response to specific features in the image data, thereby establishing a self-referencing scheme. Thus for example, as we have recently shown,

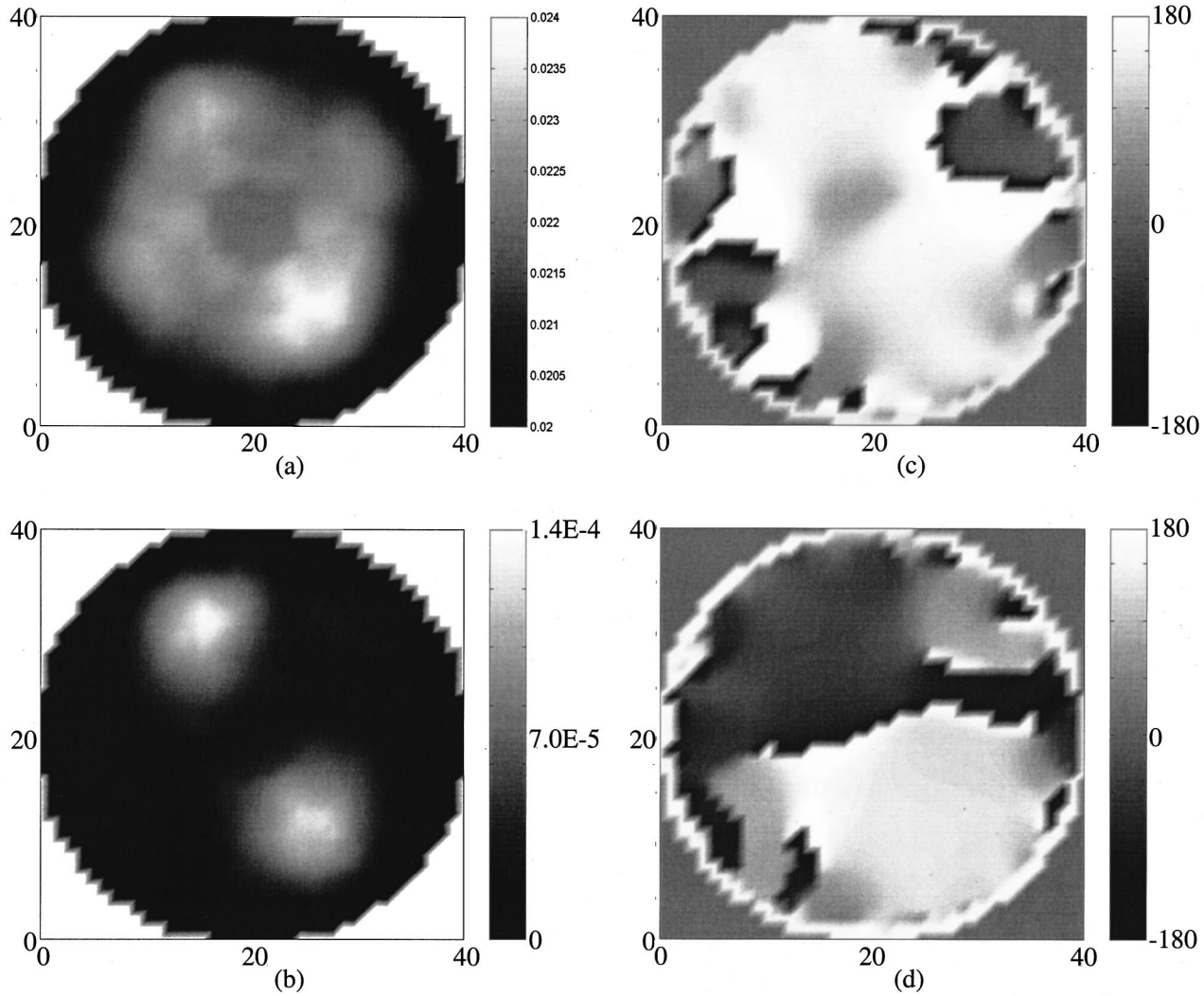

Fig. 11. Results from laboratory phantom experiment (see Figs. 2 and 3). Prior to reconstruction, each individual detector reading was normalized to the reading obtained for that detector when the balloons and frame were removed from the phantom. (a) image reconstructed from the 6 × 18 detector readings acquired at one specific time point. (b) 0.12-Hz component of the amplitude of the image sequence's DFT, 180° phase difference between oscillating balloons; (c) 0.12-Hz component of the phase of the image sequence's DFT, no phase difference between oscillating balloons; (d) 0.12-Hz component of the phase of the image sequence's DFT, 180° phase difference between oscillating balloons.

the locating of where in the cross-sectional view a cardiac frequency is found can be used to identify the position of the major arteries.[13–16] We also recognize that such measures, in addition to aiding in validating the accuracy of imaging results from tissue, can in and of themselves provide a wealth of new information regarding the state of vascular dynamics. This follows, as hemoglobin, which is usually compartmentalized in the vascular space, is a principal contrast feature of tissue in the NIR region. It is instructive to consider what might be learned from investigations of vascular dynamics by optical tomography, in particular as it relates to the quality of information derivable from alternative schemes that have been suggested for use in optical imaging.

A. Significance of Cross-Sectional Imaging of Dynamic Behavior by Optical Tomography

Vascular frequencies arise in response to cardiac, respiratory, vasomotor, and local metabolic influences. A notable feature of these is that they are not uniformly distributed among the various components of the vascular tree, but instead exhibit structure dependence. Thus, whereas the cardiac frequency is mainly restricted to arterial structures, the vasomotor and respiratory frequencies are principally limited to the microvessels and structures associated with the venous circulation, respectively. Presently, measures of these rhythms are limited mainly to investigations of vascular structures lying near the surface, primarily microvessels, by laser Doppler flowmetry,[45] or of larger subsurface vessels by Duplex ultrasonography.[46] Also available for measuring vascular rhythms is the spatially integrating method of pulse volume recording achieved using pneumoplethysmography[47] or photoplethysmography.[48] Thus far, however, the ability to spatially discriminate among the various vascular frequencies in a cross-sectional view, especially in the case of large tissue structures, has been lacking. As demonstrated by results presented here, measures of

dynamic behavior can be used to detect features with high contrast that otherwise might remain obscured owing to the limited spatial resolution. This is supported by results for the modeled tumor and by those for the laboratory phantom.

As noted, it is our view that the potential to distinguish the dynamics of different components of the vascular tree could hold considerable significance for the characterization of various physiological states and disease processes. For instance, the presence (or absence) of a cardiac frequency with respect to known anatomic landmarks (e.g., major arteries) could provide a measure of the patency of localized arterial flow. Abnormally low-amplitude signals might suggest the presence of arterial stenosis. Clinically, such measures could hold considerable value, especially in the evaluation of peripheral vascular disease of the lower extremities, a problem frequently encountered with diabetics. Presently, such measures are performed using the method of pulse volume recording.[49] This method, however, cannot identify which vessel is involved. To achieve this, x-ray angiography typically is performed, which requires the infusion of a contrast agent—a strategy not without risk, especially in patients with renal insufficiency. Imaging based on dynamic optical measurements, on the other hand, might allow for sufficient localization of the involved structure without the need for any external contrast agent. Indirect evidence that such measures may prove feasible comes from recent studies we have conducted on the human forearm. In one case, already noted, we observed that spatial maps revealing the amplitude of the cardiac frequency, derived from analysis of an image time series, coincided well with the correct locations of the radial, interosseous, and ulnar arteries.[13–16] In another study involving simultaneous measurements, we observed that graded occlusion of the brachial artery in the upper arm is accompanied by selective reduction in flow rates in the radial artery (measured by duplex ultrasonography) and by reduced blood volume in the vicinity of the radial and ulnar arteries in the forearm (measured by dynamic optical tomography).[50]

Evaluation of altered perfusion states might also prove helpful for the detection and localization of tumors, owing to their known altered vascular state.[44,51] Such measures could be aided by various homeostatic challenges that serve to alter local blood flow. Simple examples could include deep breathing,[4] mild elevation of blood pressure by exercising a handgrip,[52] or monitoring the response to a cold shock.[53] Recently, we have shown that such manipulations, all of which are significantly less invasive than, say, administration of an injectable contrast agent, can induce significant changes in the spatiotemporal dynamics of the vasculature in the human forearm.[14–16]

B. Imaging of Chaos of Vascular Dynamics

Another feature of the vascular response that is receiving increasing attention, for which dynamic optical measures could have substantial value, is the accumulating evidence that the temporal variability of vasculature is chaotic in nature.[54,55] These signatures, which are widely observed in biology, arise from nonlinear interactions of controlling variables and exhibit the property of sensitivity to initial conditions. The existence of such behavior has important implications in the understanding of disease processes as well as for the approaches taken for therapy.[56] For instance, the approach needed to control a chaotic system is quite different from that for a linear system, wherein the system response is proportional to the magnitude of the input stimulus. Thus it has been proposed that more-effective therapies can be realized from a series of well-timed perturbations rather than from the standard approach of applying a constant stimulus, the method commonly used in many pharmacological interventions.[57] Also of interest, and related to this, is the seemingly general finding that the occurrence of chaotic behavior in physiological systems is a sign of health, and its absence is a sign of disease. For instance, it is known that heart rate variability is chaotic.[58,59] Significantly, loss of this signature with the appearance of periodic oscillations is among the strongest predictors of sudden cardiac death.[59] A similar phenomenology has been observed in infants who succumb to sudden infant death syndrome.[60] In this case, the normally chaotic respiratory rate becomes periodic prior to the fatal incident. Similarly, during epileptic seizures, electroencephalographic recordings exhibit a transition from chaotic to periodic activity.[61] Presently, the capacity to monitor such behavior in vascular structures is limited principally to near-surface measures using laser Doppler methods. Measures of temporal variability in the vascular caliber and flow motion for larger vessels is possible using Duplex ultrasound, but such measures are insensitive to the activity of the microvasculature and do not provide for full cross-sectional views. Moreover, because of attenuation by the skull, they are mainly excluded from investigation of the vascular response of the brain. Optical measures, on the other hand, are quite sensitive to the microcirculation and, as we have reported, can also be used to detect the temporal variability of larger vessels.

It is our view that the ability to monitor the dynamic response of the vasculature, including the microcirculation, could have far-reaching implications for the understanding of fundamental physiological processes dependent on the vascular response, and for the understanding of disease processes and their treatment. Significantly, in this regard, we have recently demonstrated the ability to image, with high fidelity, complex coincident spatiotemporal hemodynamic states, including chaotic states, by simulation[28] and have also obtained results from dynamic imaging studies on the human forearm that are consistent with the reported nonlinear chaotic properties of the vasculature.[13-16,50]

There are still other important implications to be considered with regard to the value of measuring the time-varying properties of hemoglobin states in a cross-sectional view. For instance, the details of the measured dynamics at the various vascular frequencies need not be the same for measures of blood volume and blood oxygenation. In addition, given the known heterogeneity of tissue perfusion,[62] even in healthy tissue, it seems likely that whatever features do exist will themselves be spatially varying. Moreover, in a case where altered dynamics in either parameter is found, it could indicate altered local metabolic states, the existence of more central con-

trol deficits (e.g., autonomic, cardiac or respiratory), or both. Hence it would seem that the suggested measures could provide for an assessment of an integrated physiological state, and possess important features pertaining to tissue/vascular coupling. In fact, it also seems likely that whatever spatiotemporal features exist will respond to a host of pharmacological agents and other treatment modalities. Such measures could also serve to identify desired or undesired responses to therapy.

C. Strategies for Data Collection

The implications of the preceding discussion notwithstanding, given the known technical and mathematical difficulties associated with optical tomography, an inclination to regard the temporal variability of tissue as an undesirable feature that should be experimentally minimized or averaged out is perhaps understandable. Several factors combine to make this an apparently sensible way to proceed. For example, many of the optical tomographic methods proposed in the past decade have been analoges of techniques (e.g., diffraction tomography) that were initially developed for use in applications where the medium under investigation *is* effectively static. Further, in other medical imaging modalities already in clinical use, either static anatomical information is that which is sought (e.g., x-ray CT, MRI), or the required data acquisition time is long relative to the time scale of most physiological fluctuations (e.g., PET,[63] SPECT[64]). [65] The issue of time scale raises the question of which measurement type, static or dynamic, is better suited for optical imaging studies of tissues.

As in other imaging modalities, which is more suitable will depend strongly on the expected temporal variance of the contrast features under investigation. If these are time invariant, then the acquisition time is often not a critical parameter. Limited acquisition times are frequently considered as a matter of convenience. Alternatively, if the contrast of the features of interest exhibits significant temporal variability, then considerations of acquisition time can be important. For instance, measurements performed on a time frame that is much longer than the time scale of the temporal fluctuations will produce effectively blurred, low-contrast images having degraded information value (i.e., low diagnostic sensitivity and specificity). In this regard, many of the data collection strategies proposed for optical tomography are poorly suited to acquire detector readings on a time scale that measurement of dynamic properties of tissue would demand. This limitation is present, for instance, in techniques that are based upon measurement of the temporal spread of light pulses, or on related parameters such as the mean time of flight.[66,67] While the temporal point spread function in principle provides the most and best information possible from which to deduce the internal structure of a scattering medium, the practical requirement for signal averaging in the case of large tissue structures imposes acquisition times on a time scale of minutes. The difficulty with this is that it conflicts with well-known features of vascular physiology, in particular the vasomotor response. This is characterized by perfusion of first one region, then another. Eliminating its influence by adopting time-averaging methods will adversely impact on the available contrast due to hemoglobin, which is the very feature many seek to measure. In fact, we suspect that this is what accounts for the nearly complete absence of absorption contrast in the cross-sectional optical images of the forearm recently presented by Hillman *et al.*,[10] who reported requiring several minutes to complete a single scan.

In contrast, a dc measurement, while theoretically less informative than a time-resolved measurement,[68] has the advantage that it can allow for tomographic measurements on a time scale much shorter than that of the temporal variations in the vascular response. In fact, we have recently described instrumentation based on such measures that are well suited for dynamic imaging studies.[12]

An alternative to time averaging and dynamic measures is to collect data on a time scale that is fast compared with the underlying variability of target contrast, a so-called snapshot. While technically achievable, the obvious difficulty with this lies in the expected variance of any measure. We mention this because in addition to the influence of vascular rhythms, a well-known feature of the vascular response is its considerable sensitivity to autonomic stimuli. This can take on many forms. A cool breeze, a sudden startle, pain, embarrassment, loud noise, and related stimuli are all known to produce an abrupt autonomic response leading in many instances to global vasoconstriction of superficial vessels, especially those in the skin, with concomitant deep-vessel vasodilation. We have confirmed the sensitivity of our measuring technology to such provocations (specifically, a cold shock) and have observed large local amplitude variations ($\sim$300%) in tissue blood volume in the forearm within $<$2 s of onset of stimuli. Because such reactions frequently occur or are easily induced, it would seem appropriate that close attention be paid to the environmental conditions under which optical measurements are made. Certainly this is a common practice in clinical EEG studies. Absent this, it is hard to imagine how repeatable results could be obtained, particularly in the case of discrete measures. Taken together, we believe that the considerations outlined above render it likely that dynamic measures will provide the highest quality information.

D. Some Further Considerations

1. Computational limits

An obvious concern regarding the suitability of dynamic measures is the computational burden it may entail. Indeed, while the time required for computing a series of images scales linearly with the number of images, it is not always necessary to first compute the image series in order to extract dynamic features. Instead, specific features can be derived first from the time-varying detector data and images of these parameters subsequently computed directly. An example of an operation that is commutative with the imaging operator is the DFT. In fact, a range of linear operations can be similarly applied. Another of interest is the identification of the principal components of a time series,[69] a technique which has been applied, for example, by Mayhew *et al.* to evaluate time-

varying surface reflectance measures of rat brain following a specific challenge.[70] In an imaging modality, such measures can directly provide spatial maps that reveal the evolution of specific features over time, a capability likely to have considerable utility in the detection of focal disturbances in vascular states.

The ability to extract desired features directly from the detector data, however, requires commutativity of the imaging and time-series analysis operators. Of the specific operations considered in this report, those that involve comparisons between time series in different pixels do not satisfy this condition. Thus the DFT maps presented in Figs. 7 and 8 could also have been produced (as confirmed in results not shown) by reconstructing the 0.06- and 0.52-Hz components, respectively, of the DFTs of the detector readings, while the CSD and coherence maps shown in Figs. 9 and 10 could not have been. However, as indicated by Eqs. (5) and (6), indirect estimates of these quantities at a given frequency can be derived from a reconstructed DFT component.[33] While in practice, as described above in Subsection 2.C, this would entail dividing the detector data time series in some number $n_d > 1$ of "records" and performing a separate DFT computation and reconstruction based on the data in each one, the total computational burden could still be substantially less than that associated with reconstructing a complete time series of images. No such savings is possible for the cross-correlation function, however, which *can* be obtained by computing a finite inverse Fourier transform of a CSD, but only if estimates of the latter are available over the entire range of frequencies for which it is defined (see Subsection 2.C).[33]

2. Stability of Derived Measures

Although not directly examined here, an issue of practical concern having an impact on the suitability of dynamic measures is the stability of derived information, given the range of uncertainties associated with both data collection and data analysis. Unlike many well-established physiological measurement techniques, information regarding target features obtained by reconstruction methods is obtained indirectly. One consequence of this is that, depending on the numerical methods used and the type of information evaluated, the stability of reconstructed images to simplifying assumptions can vary considerably. For instance, we have recently explored the sensitivity of reconstructed images of absolute coefficient values, images of relative changes in these compared to some defined state, and spatial maps of dynamic features derived from the latter, to the influence of inaccuracies in the initial guess within the framework of a first-order solution using linear perturbation theory (i.e., methods employed here).[28] These studies have shown that the accuracy of derived measures in the presence of such errors varies according to the following inequality: absolute measures $\ll$ relative measures $<$ dynamic measures. In these and other studies,[13–16] we have found that maps revealing dynamic features can be computed with remarkable accuracy even if the quality of the image time series from which these measures were derived has significantly poorer quality. This finding coincides well with the demonstration made here that features present in the optical coefficient or hemodynamic parameter images, but obscured because of low spatial resolution, can be revealed with considerable accuracy and high contrast from examination of dynamic properties.

This marks an important distinction between varieties of optical tomography in which detector readings are highly scattered, and others in which the properties and dimensions of the target media permit reconstruction by methods based on the Radon transform. An instructive example of the latter type of optical tomography is the imaging of jets of heated air that flow through a ring of sources and detectors.[71] Although the authors of Ref. 71 do not explicitly show any data obtained by performing time-series analysis operations such as those we have employed, the capability of doing so clearly exists. However, it is important to note that their method fundamentally is a type of standard straight-line tomography. Only the detector diametrically opposite a given source receives light from that source. Consequently, the individual images in the time series contain high-quality information in themselves, comparable to the quality of any additional information that could be extracted through time-series analysis operations. This stands in sharp contrast to the results that have been presented here for diffuse optical tomography, wherein the feature contrast and spatial resolution of the derived dynamic features are, in many instances, considerably improved compared to those of the optical or hemodynamic parameter images from which they were derived.

3. Other Numerical Considerations

A fact already known to many but worth emphasizing is that considerable flexibility exists regarding the determination of specific features from a system, given time-series data. In many situations it is possible not only to identify the *presence* of specific features, but also to, in a certain manner, emphasize their *absence*. An example of what is meant by this can be seen in Fig. 12, which shows an overlay of the DFT amplitudes of the time-

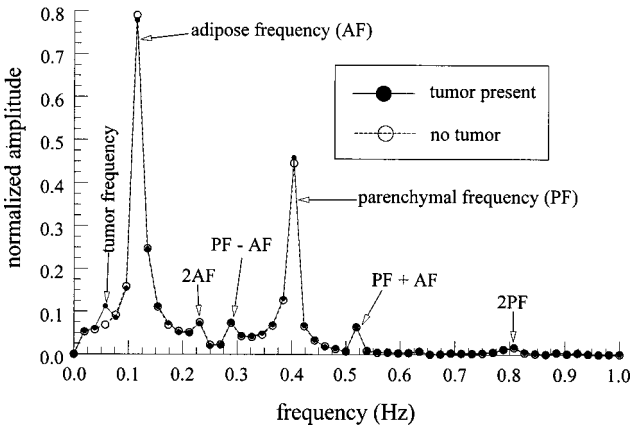

Fig. 12. Amplitude of the discrete DFTs of a representative detector readings time series, for the model medium with (solid curve, solid circles) and without (dashed curve, open circles) the tumor. Strong peaks are present at the adipose frequency (0.12 Hz) and the parenchyma frequency (0.4 Hz) for both target media, while a peak at the tumor frequency (0.06 Hz) occurs only in the tumor-bearing medium. Peaks also are seen at overtone and mixing frequencies.

varying detector values for a detector positioned opposite the source and obtained from the MR-derived target medium in the presence of and in the absence of the tumor. To facilitate comparison, the detector readings were high-pass filtered to remove their dc components, and then normalized to unit sum-of-squares (i.e., unit spectral energy). The contribution of the tumor to the Fourier amplitude spectrum is explicitly pointed out in the figure. It is seen that this component has a small amplitude and, even worse, it lies inside a "tail" of the much stronger adipose peak.[72] Consequently, it could be expected that detecting the tumor and accurately characterizing its location and size would be difficult to accomplish if it had to be done directly on the basis of characteristic signals arising from the tumor tissue. But in fact there is no such necessity, for it is possible to derive feature maps that are very sensitive to the *absence* of the higher-amplitude frequencies of the other two tissue types at locations where the tumor has displaced them. In fact, this phenomenon is responsible for the remarkable contrast and spatial accuracy seen in the coherence images shown in Fig. 10. These results were obtained at 0.54 Hz, which is (within the numerical limitations of the calculation) the sum of the adipose and parenchyma frequencies. This frequency is present outside the tumor and absent within it.

5. CONCLUSION

Optical tomography, in its present form, produces images having relatively low spatial resolution. Because image artifacts can be expected, efforts to separate these from true features could prove difficult, especially in the case of tissue studies where the background optical properties are mainly unknown and likely time-varying, owing to vascular reactivity. As discussed, measures of certain vascular rhythms, or related phenomena, may allow for the independent validation of specific features. This can serve not only as a qualitative check on the accuracy of images and feature maps, but in addition the derived temporal features themselves, whether naturally occurring or induced, can reveal features of functional activity having contrast and spatial resolution superior to that found in any discrete-time image. Thus measures of optical properties of tissue are useful not only for their intrinsic information content, but also as indicators of changes and rates of change in perfusion. Analysis of this information in an imaging modality holds promise for opening new vistas in understanding integrated physiological states, as well as providing new measures for diagnostic and monitoring purposes.

ACKNOWLEDGMENT

This work was supported in part by National Institutes of Health grant RO1-CA66184.

Correspondence should be addressed to Randall L. Barbour at rbarbour@netmail.hscbklyn.edu. http://138.5.51.241/index/.

REFERENCES AND NOTES

1. B. Chance, R. R. Alfano, B. J. Tromberg, M. Tamura, and E. M. Sevick-Muraca, eds., *Optical Tomography and Spectroscopy of Tissue IV*, Proc. SPIE **4250** (2001).
2. H. Liu, D. A. Boas, Y. Zhang, A. G. Yodh, and B. Chance, "Determination of optical properties and blood oxygenation in tissue using continuous NIR light," Phys. Med. Biol. **40**, 1983–1993 (1995).
3. H. Liu, B. Chance, A. H. Hielscher, S. L. Jacques, and F. K. Tittel, "Influence of blood vessels on the measurement of hemoglobin oxygenation as determined by time-resolved reflectance spectroscopy," Med. Phys. **22**, 1209–1217 (1995).
4. J. W. Covell, "Cardiovascular control and integrated responses," in (Best and Taylor's) *Physiological Basis of Medical Practice*, 11th ed., J. B. West, ed. (Williams and Wilkins, Baltimore, Md., 1985), Chap. 16.
5. C. E. Elwell, R. Springett, E. Hillman, and D. T. Delpy, "Oscillations in cerebral haemodynamics," in *Oxygen Transport to Tissue XXI*, Vol. 471 of Advances in Experimental Medicine and Biology, A. Eke and D. T. Delpy, eds. (Kluwer Academic/Plenum, New York, 1999), pp. 57–65.
6. J. E. W. Mayhew, S. Askew, Y. Zheng, J. Porrill, G. W. M. Westby, P. Redgrave, D. M. Rector, and R. M. Harper, "Cerebral vasomotion: a 0.1-Hz oscillation in reflected light imaging of neural activity," Neuroimage **4**, 183–193 (1996).
7. M. A. Franceschini, V. Toronov, M. E. Filiaci, E. Gratton, and S. Fantini, "On-line optical imaging of the human brain with 160-ms temporal resolution," Opt. Express **6**, 49–57 (2000). http://www.opticsexpress.org.
8. A. Zourabian, A. Siegel, B. Chance, N. Ramanujan, M. Rode, and D. A. Boas, "Trans-abdominal monitoring of fetal arterial blood oxygenation using pulse oximetry," J. Biomed. Opt. **5**, 391–405 (2000).
9. A. Villringer and B. Chance, "Non-invasive optical spectroscopy and imaging of human brain function," Trends Neurosci. **20**, 435–442 (1997).
10. E. M. C. Hillman, J. C. Hebden, F. E. W. Schmidt, S. R. Arridge, M. E. Fry, M. Schweiger, and D. T. Delpy, "Initial clinical testing of the UCL 32 channel time-resolved instrument for optical tomography," in *Biomedical Topical Meetings*, OSA Technical Digest (Optical Society of America, Washington D.C., 2000), pp. 100–102.
11. T. O. McBride, B. W. Pogue, E. D. Gerety, S. B. Poplack, U. L. Österberg, and K. D. Paulsen, "Spectroscopic diffuse optical tomography for the quantitative assessment of hemoglobin concentration and oxygen saturation in breast tissue," Appl. Opt. **38**, 5480–5490 (1999).
12. C. H. Schmitz, H. L. Graber, H. Luo, I. Arif, J. Hira, Y. Pei, A. Bluestone, S. Zhong, R. Andronica, I. Soller, N. Ramirez, S.-L. S. Barbour, and R. L. Barbour, "Instrumentation and calibration protocol for imaging dynamic features in dense-scattering media by optical tomography," Appl. Opt. **39**, 6466–6486 (2000).
13. H. L. Graber, C. H. Schmitz, Y. Pei, S. Zhong, S.-L. S. Barbour, S. Blattman, T. Panetta, and R. L. Barbour, "Spatiotemporal imaging of vascular reactivity," in *Physiology and Function from Multidimensional Imaging*, A. V. Clough and C.-T. Chen, eds., Proc. SPIE **3978**, 32–43 (2000).
14. H. L. Graber, S. Zheng, Y. Pei, C. H. Schmitz, I. Arif, J. Hira, and R. L. Barbour, "Dynamic imaging of muscle activity by optical tomography," in *Biomedical Topical Meetings*, OSA Technical Digest (Optical Society of America, Washington, D.C., 2000), pp. 407–408.
15. R. L. Barbour, H. L. Graber, S. Zheng, Y. Pei, J. Hira, and I. Arif, "Optical imaging of the response of vascular dynamics to a cold shock," in *Biomedical Topical Meetings*, OSA Technical Digest (Optical Society of America, Washington, D.C., 2000), pp. 430–432.
16. S. Blattman, H. L. Graber, S. Zheng, Y. Pei, J. Hira, I. Arif, and R. L. Barbour, "Imaging of differential reactivity of the vascular tree in the human forearm by optical tomography," in *Biomedical Topical Meetings*, OSA Technical (Optical Society of America, Washington D.C., 2000), pp. 458–460.

17. D. W. Fawcett, *Bloom and Fawcett's A Textbook of Histology*, 12th ed. (Chapman & Hall, New York, 1994).
18. J. Folkman, "Angiogenesis and breast cancer," J. Clin. Oncol. **12**, 441–443 (1994).
19. C. W. Song, A. Lokshina, J. G. Rhee, M. Patten, and S. H. Levitt, "Implication of blood flow in hyperthermic treatment of tumors," IEEE Trans. Biomed. Eng. **31**, 9–16 (1984).
20. T. L. Troy, D. L. Page, and E. M. Sevick-Muraca, "Optical properties of normal and diseased breast tissues: prognosis for optical mammography," J. Biomed. Opt. **1**, 343–355 (1996).
21. A. H. Hielscher, R. E. Alcouffe, and R. L. Barbour, "Comparison of finite-difference transport and diffusion calculations for photon migration in homogeneous and heterogeneous tissues," Phys. Med. Biol. **43**, 1285–1302 (1998).
22. O. W. van Assendelft, *Spectrophotometry of Haemoglobin Derivatives*, (Thomas, Springfield, Ill., 1970).
23. H. J. van Staveren, C. J. M. Moes, J. van Marle, S. A. Prahl, and M. J. C. van Gemert, "Light scattering in Intralipid-10% in the wavelength range of 400-1100 nm," Appl. Opt. **30**, 4507–4514 (1991).
24. I. Driver, J. W. Feather, P. R. King, and J. B. Dawson, "The optical properties of aqueous suspensions of Intralipid, a fat emulsion," Phys. Med. Biol. **34**, 1927–1930 (1989).
25. S. T. Flock, S. L. Jacques, B. C. Wilson, W. M. Star, and M. J. C. van Gemert, "Optical properties of Intraplipid: a phantom medium for light propagation studies," Lasers Surg. Med. **12**, 510–519 (1992).
26. G. M. Hale and M. R. Querry, "Optical constants of water in the 200-nm to 200-μm wavelength region," Appl. Opt. **12**, 555–563 (1973).
27. R. L. Barbour, R. Andronica, Q. Sha, H. L. Graber, and I. Soller, "Development and evaluation of the IRIS-OPTIscanner, a general-purpose optical tomographic imaging system," in *Advances in Optical Imaging and Photon Migration* J. G. Fujimoto and M. S. Patterson, eds., Vol. 21 of OSA Trends in Optics and Photonics Series (Optical Society of America, Washington, D.C., 1998), pp. 251–255.
28. Y. Pei, H. L. Graber, and R. L. Barbour, "Influence of systematic errors in reference states on image quality and on stability of derived information for DC optical imaging," Appl. Opt. **40**, 5755–5769 (2001).
29. H. L. Graber, Y. Pei, and R. L. Barbour, "Imaging of spatiotemporal coincident states by dynamic optical tomography," in Ref. 1, pp. 153–163.
30. R. L. Barbour, H. L. Graber, Y. Pei, and C. H. Schmitz, "Imaging of vascular chaos," in Ref. 1, pp. 577–590.
31. *Using MATLAB Version 5*, (The Mathworks, Inc., Natick, Mass., 1998) Chap. 5; http://www.mathworks.com/access/helpdesk/help/techdoc/ref/griddata.shtml.
32. Ref. 31; http://www.mathworks.com/access/helpdesk/help/techdoc/ref/delaunay.shtml.
33. J. S. Bendat and A. G. Piersol, *Engineering Applications of Correlation and Spectral Analysis*, 2nd ed. (Wiley, New York, 1993).
34. G. M. Jenkins and D. G. Watts, *Spectral Analysis and its Applications* (Holden-Day, Oakland, Calif., 1968).
35. *Signal Processing Toolbox User's Guide (Version 4)* (The Mathworks, Inc., Natick, Mass., 1998) Chap. 6; http://www.mathworks.com/access/helpdesk/help/toolbox/signal/fft.shtml.
36. Ref. 35; http://www.mathworks.com/access/helpdesk/help/toolbox/signal/xcorr.shtml.
37. As the temporal variations of the target media used in the studies considered here were perfectly periodic, the length and number of records can be set to any desired value. The effects of record number and length (and also other considerations such as filtering and windowing) lie outside the scope of the present report.
38. Ref. 35; http://www.mathworks.com/access/helpdesk/help/toolbox/signal/csd.shtml.
39. Ref. 35; http://www.mathworks.com/access/helpdesk/help/toolbox/signal/csd.shtml.
40. The last interpretation given is particularly intriguing for us, as it immediately brings to mind an analogy between this general concept of signal coherence and the particular physical meaning of "coherence" that applies to light. It suggests that the "coherence radius" and "coherence time" that could be defined for each pixel in an image time series may be parameters worth considering.
41. M. Schweiger, S. R. Arridge, and D. T. Delpy, "Application of the finite-element method for the forward and inverse models in optical tomography," J. Math. Imag. Vision **3**, 263–283 (1993).
42. H. Jiang, K. D. Paulsen, U. L. Österberg, and M. S. Patterson, "Frequency-domain optical image reconstruction in turbid media: an experimental study of single-target detectability," Appl. Opt. **36**, 52–63 (1997).
43. V. Ntziachristos, B. Chance, and A. G. Yodh, "Differential diffuse optical tomography," Opt. Express **5**, 230–242 (1999), http://www.opticsexpress.org.
44. P. Vaupel, "Vascularization, blood flow, oxygenation, tissue pH, and bioenergetic status of human breast cancer," in *Oxygen Transport to Tissue XVIII (Advances in Experimental Medicine and Biology)* E. M. Nemoto and J. C. LaManna, eds. (Plenum, New York, 1997), Vol. 411, pp. 243–254.
45. S. Sunberg and M. Castrén, "Drug- and temperature-induced changes in peripheral circulation measured by laser-Doppler flowmetry and digital-pulse plethysmography," Scand. J. Clin. Lab. Invest. **46**, 359–365 (1986).
46. C. Holvombe, N. Pugh, K. Lyons, A. Douglas-Jones, R. E. Mansel, and K. Horgan, "Blood flow in breast cancer and fibroadenoma estimated by colour Doppler ultrasonography," Br. J. Surg. **82**, 787–788 (1995).
47. A. T. Johnson, C. G. Lausted, and J. D. Bronzino, "Respiratory system," in *The Biomedical Engineering Handbook*, 2nd ed., J. D. Bronzino, ed. (CRC Press, Boca Raton, Fla., 2000), Chap. 7.
48. M. H. Sherebrin and R. Z. Sherebrin, "Frequency analysis of the peripheral pulse wave detected in the finger with a photoplethysmograph," IEEE Trans. Biomed. Eng. **37**, 313–317 (1990).
49. G. Drzewiecki, "Noninvasive arterial blood pressure and mechanics," in *The Biomedical Engineering Handbook*, 2nd ed., J. D. Bronzino, ed. (CRC Press, Boca Raton, Fla., 2000), Chap. 71.
50. S. Blattman, H. L. Graber, S. Zheng, Y. Pei, J. Hira, I. Arif, and R. L. Barbour, "Imaging of tissue reperfusion by dynamic optical tomography," in *Biomedical Topical Meetings*, OSA Technical Digest (Optical Society of America, Washington D.C., 2000), pp. 409–410.
51. B. Endrich and P. Vaupel, "The role of the microcirculation in the treatment of malignant tumors: facts and fiction," in *Blood Perfusion and Microenvironments of Human Tumors: Implications for Clinical Radiooncology*, M. Molls and P. Vaupel, eds. (Springer–Verlag, Berlin, 1998), pp. 19–39.
52. C. Sohn, F. Beldermann, H. Frey, S. Reinhart, J. Sohn, and G. Bastert, "Durchblutungsdiagnostik von Mammatumoren unter Blutdruckerhöhung: neue Möglichkeiten in der Dignitätsdiagnostik," Radiologe **37**, 643–650 (1997).
53. C. Franssen, H. Wollershein, A. de Haan, and T. Thien, "The influence of different beta-blocking drugs on the peripheral circulation in Raynaud's phenomenon and in hypertension," J. Clin. Pharm. **32**, 652–659 (1992).
54. D. T. Kaplan and A. L. Goldberger, "Chaos in cardiology," J. Cardiovasc. Electrophys. **2**, 342–354 (1991).
55. T. M. Griffith, "Chaos and fractals in vascular biology," Vasc. Med. Rev. **5**, 161–182 (1994).
56. J. Bélair, L. Glass, U. an der Heiden, and J. Milton, "Dynamical disease: identification, temporal aspects and treatment strategies of human illness," Chaos **5**, 1–7 (1995).
57. J. N. Weiss, A. Garfinkel, M. L. Spano, and W. L. Ditto, "Chaos and chaos control in biology," J. Clin. Invest. **93**, 1355–1360 (1994).
58. J. K. Kantors, M. V. Højgaard, E. Agner, and N.-H. Holstein-Rathlou, "Short- and long-term variations in nonlinear dynamics of heart rate variability," Cardiovasc. Res. **31**, 400–409 (1996).

59. P. Mansier, J. Clairambault, N. Charlotte, C. Médigue, C. Vermeiren, G. LePape, F. Carré, A. Gounaropoulou, and B. Swynghedauw, "Linear and non-linear analyses of heart rate variability: a minireview," Cardiovasc. Res. **31**, 371–379 (1996).
60. S. F. Glotzbach, R. L. Ariagno, and R. M. Harper, "Sleep and the sudden infant death syndrome," in *Principles and Practice of Sleep Medicine in the Child*, R. Ferber and M. H. Kryger, eds. (Saunders, Philadelphia, Pa., 1995), pp. 231–244.
61. J. Theiler, "On the evidence for low-dimensional chaos in an epileptic electroencephalogram," Phys. Lett. A **196**, 334–341 (1995).
62. C. G. Ellis, S. M. Wrigley, and A. C. Groom, "Heterogeneity of red blood cell perfusion in capillary networks supplied by a single arteriole in resting skeletal muscle," Circ. Res. **75**, 357–368 (1994).
63. T. F. Budinger and H. F. VanBrocklin, "Positron-emission tomography (PET)," in *The Biomedical Engineering Handbook*, 2nd ed., J. D. Bronzino, ed. (CRC Press, Boca Raton, Fla., 2000), Chap. 67.
64. B. Y. Croft and B. M. W. Tsui, "Nuclear medicine," in *The Biomedical Engineering Handbook*, 2nd ed., J. D. Bronzino, ed. (CRC Press, Boca Raton, Fla., 2000), Chap. 64.
65. EEG and MEG imaging techniques have temporal resolutions sufficiently fine to respond to variations resulting from the respiratory and cardiac cycles, but these are limited to functional studies of the brain; even here, their purpose is to assess neuronal, not circulatory, function.
66. R. R. Alfano, S. G. Demos, P. Galland, S. K. Gayen, Y. Guo, P. P. Ho, X. Liang, F. Liu, L. Wang, Q. Z. Wang, and W. B. Wang, "Time-resolved and nonlinear optical imaging for medical applications," in *Advances in Optical Biopsy and Optical Mammography,* Vol. 838 of the Annals of the New York Academy of Sciences (New York Academy of Sciences, New York, 1998), pp. 14–27.
67. K. Wells, J. C. Hebden, F. E. W. Schmidt, and D. T. Delpy, "The UCL multichannel time-resolved system for optical tomography," in *Optical Tomography and Spectroscopy of Tissue: Theory, Instrumentation, Model, and Human Studies II*, B. Chance and R. R. Alfano, eds., Proc. SPIE **2979**, 599–607 (1997).
68. S. R. Arridge and W. R. B. Lionheart, "Nonuniqueness in diffusion-based optical tomography," Opt. Lett. **23**, 882–884 (1998).
69. I. T. Joliffe and B. J. T. Morgan, "Principal component analysis and exploratory factor analysis," Stat. Meth. Med. Res. **1**, 69–95 (1992).
70. J. Mayhew, D. Hu, Y. Zheng, S. Askew, Y. Hou, J. Berwick, P. J. Coffey, and N. Brown, "An evaluation of linear model analysis techniques for processing images of microcirculation activity," Neuroimage **7**, 49–71 (1998).
71. L. McMackin, R. J. Hugo, R. E. Pierson, and C. R. Truman, "High speed optical tomography system for imaging dynamic transparent media," Opt. Express **1**, 302–311 (1997). http://www.opticsexpress.org.
72. While addition of a spectral windowing operation to the time-series analysis would likely yield better frequency resolution than that seen in this figure, none was actually used while the results presented in this report were being generated.